Journal of the Meteorological Society of Japan

EARLY ONLINE RELEASE

The DOI for this manuscript is
DOI:10.2151/jmsj.2022-049
J-STAGE Advance published date: September 14th, 2022
The final manuscript after publication will replace the preliminary version at the above DOI once it is available.

Resolution Impact on Rapid Intensification and Structure Change of Super Typhoon Hagibis (2019)

Hao Jin, Jonathan R. Moskaitis, Yi Jin, and James D. Doyle

U.S. Naval Research Laboratory, Monterey, CA, USA

Revised Version 5

August 2022

Submitted to special edition "Typhoons in 2018–2019"

Journal of the Meteorological Society of Japan

Corresponding author address: Hao Jin, Naval Research Laboratory, 7 Grace Hopper Ave., Monterey, CA 93943. Email: hao.jin@nrlmry.navy.mil

Keywords: Tropical Cyclone, Typhoon, Rapid Intensification, Secondary Eyewall Formation, Eyewall Replacement Cycle, Resolution, Grid Spacing.

Abstract

Typhoon Hagibis (2019) was a large and intense tropical cyclone that had significant societal impacts in Japan. It went through a period of explosive rapid intensification (RI), with an increase of maximum wind speed from 60 kt to 160 kt in 24 h, immediately followed by a secondary eyewall formation (SEF) and an eyewall replacement cycle (ERC). Operational forecasts from COAMPS-TC (Coupled Ocean/Atmosphere Mesoscale Prediction System – Tropical Cyclone) failed to capture Hagibis' explosive RI, peak intensity, and the associated inner-core structural evolution. Four COAMPS-TC sensitivity experiments, initialized at 1200 UTC 5 Oct. 2019, were conducted to study the impact of horizontal resolution on prediction of Typhoon Hagibis' RI and structure. Results indicate that rapid intensification of the storm to Category 4 intensity can be simulated with the finest grid spacing at 4-km, but use of 1.33-km for the finest grid spacing facilitates more realistic prediction of the explosive intensification rate, Category 5 peak intensity, and small inner core accompanying the RI. Our sensitivity experiments indicate that realistic simulation of Hagibis' SEF/ERC requires a very intense storm with a small inner core as a prerequisite for its occurrence; therefore the finest grid spacing at 1.33-km is a necessary but not sufficient to capture the SEF/ERC. The simulation of the RI and SEF/ERC is also sensitive to the resolution of the outermost grid, which has impacts on the storm's moisture distribution by modulating the flow of moist air from the deep tropics into the TC. While these results have implications for the grid configuration of operational models like COAMPS-TC, additional work is needed to gain systematic understanding of the physical processes associated with simulation of explosive RI and SEF/ERC.

1. Introduction

Super Typhoon Hagibis was the strongest typhoon to strike mainland Japan in decades and one of the largest typhoons ever recoded, with a peak of gale-force wind diameter of 1529 km (Japan Meteorological Agency 2020). Hagibis had significant societal impacts with intense winds and more than 35 inches (1 inch = 2.54 cm) of precipitation in 24 hours causing landslides and devastating floods, leading to a mass evacuation of 3.9 million people and 432,000 households without power (New York Times 2019). Hagibis caused 99 deaths and $15B (USD) in damage in Japan, making it the costliest typhoon on record there (AON 2020).

The tropical disturbance that became Hagibis formed on 4 Oct. 2019 northwest of the Marshall Islands in the Western North Pacific Ocean[1]. It became a tropical depression on 5 Oct. and moved westward toward the Northern Mariana Islands as it began to rapid intensify. A period of explosive rapid intensification (RI) occurred on 6 Oct. as the storm developed a very small inner core in a highly favorable environment of warm sea surface temperatures (SST) and low vertical wind shear. Tropical cyclone heat potential, a measure of oceanic heat content, was high (with a peak over 100 kJ cm^{-2}) along the path of Hagibis (Wada and Chan 2021), which provided a conducive oceanic state for Hagibis to advance to Category 5. Hagibis became a super typhoon by early on Oct. 7 and reached peak intensity at 1200 UTC 7 Oct., with maximum wind speed (MWS) of 160 kt (82 m s^{-1}) and a minimum sea-level pressure (MSLP) of 890 hPa. In the 24 h ending at the time of peak intensity Hagibis intensified by a remarkable 100 kt of MWS and a drop of 98 hPa of MSLP, easily exceeding the 30 kt / 24 h or 42 hPa / 24 h intensification rates typically considered as the threshold for RI (Kaplan and DeMaria 2003, Holiday and Thompson 1979). Just after the time of peak intensity the storm passed through the Northern Mariana Islands. Hagibis then moved northwestward and underwent an eyewall replacement cycle (ERC), in which its very small inner core dissipated and was replaced by a new eyewall at a larger radius. During the ERC the intensity dipped to 120 kt, but by 1800 UTC Oct. 8 the new eyewall was well-established and the storm re-attained super typhoon status. After this time, Hagibis moved generally northwards towards Japan as a large and intense typhoon.

To accurately predict the RI and ERC of a tropical cyclone (TC) such as Super Typhoon Hagibis is a major challenge for operational TC prediction models (Jin et al. 2019). In general, the real-time operational forecasts failed to capture Hagibis' 160 kt peak intensity as well as the

[1] Storm history according to the Joint Typhoon Warning Center (JTWC) final best track

extreme RI period leading up to peak intensity. For example, Figure 1 shows operational intensity forecasts for the 1200 UTC 05 Oct. 2019 initial time. The Hurricane Weather Research and Forecast System (HWRF) regional dynamical model did the best in terms of intensifying the storm at early lead times, but still only reached a peak intensity of 120 kt. The CTCX regional dynamical model (CTCX is the operational version of COAMPS-TC using National Oceanic and Atmospheric Administration (NOAA) Global Forecast System (GFS) initial and boundary conditions) and Decay Statistical Hurricane Intensity Prediction Scheme (DSHP) both reached a higher peak intensity than HWRF, but not until after 96 h lead time. None of the models represented in Fig. 1 clearly show a sharp increase in intensity during the explosive RI, followed by a sudden decrease in intensity that accompanied the ERC, and subsequent re-intensification.

Intensification of TCs is challenging to predict, and RI is even more difficult to capture due to its sudden onset and rapid evolution. Various dynamic and thermodynamic processes are believed to play important roles in TC intensification. Emanuel (1986, 1994, 2003) proposed the wind-induced surface heat exchange (WISHE) mechanism to explain the positive feedback between the near-surface wind speed and the surface enthalpy fluxes from the underlying ocean during intensification. The various paradigms of TC intensification have been reviewed by Montgomery and Smith (2014), in which the authors argued for a more consistent treatment of both dynamic and thermodynamic processes. Gopalakrishnan et al. (2011) suggested that the horizontal resolution to resolve convection is important for the structure and intensity changes in TCs using HWRF. Jin et al. (2014) demonstrated that horizontal resolution is crucial for preserving Rossby wave energy in the TC core region and fine enough grid spacing ($\leq$ 3 km) to resolve convection.

A secondary (concentric) eyewall, often identified as a secondary convective ring with a secondary tangential wind maximum outside the primary inner eyewall, is one of the important characteristics in intense TCs (Wang et. al 2016). Despite various hypotheses that attempt to explain secondary eyewall formation (SEF), it remains elusive why hurricanes develop secondary eyewalls and ERC. Montgomery and Kallenbach (1997) suggested that vortex Rossby waves may contribute to SEF. Zhu et al. (2004) showed that an outer spiral rainband becomes a concentric secondary eyewall as Hurricane Bonnie (1998) moved from a high- to a weak-sheared environment. Wu et al. (2012) simulated a concentric eyewall formation for Typhoon Sinlaku and Huang et al. (2012) suggested that it resulted from a broadening of the tangential winds, an increase of blocking of the boundary layer (BL) inflow, and formation of enhanced surface convergence outside the primary eyewall. Abarca and Montgomery (2013, 2014, 2015) and Wang et al. (2016) suggested that the balanced dynamics underestimates the secondary circulation and the spinup of tangential winds in the primary and secondary circulations. The outer rainband convection and subgrid-scale processes are found to play important roles in ERC (Zhu and Zhu 2014; Zhu et al. 2015; Zhu 2015). Most of those SEFs studied occurred as/after the TC reached peak intensity.

The real-time CTCX forecasts issued in 2019 for Hagibis used a model configuration with a fixed outer grid at 36 km spacing and storm-following moving nested grids at 12 km and 4 km grid spacing. Although the 36/12/4 km configuration can rapidly intensify a TC, it is very likely the horizontal resolution of this model configuration is insufficient to simulate the small inner-core structure that accompanied Hagibis' extreme RI. It is also unclear from our experience with the 36/12/4 km version of CTCX that the model can realistically form a secondary eyewall and complete an ERC with that grid spacing. Thus for this study, we performed retrospective forecasts of Hagibis with the Coupled Ocean/Atmosphere Mesoscale Prediction System – Tropical Cyclone (COAMPS-TC®[2]), using grid spacing as small as 1.33 km in the region containing the TC inner core. We also performed COAMPS-TC forecast experiments in which the changed the outer grid spacing from 36 km to 12 km, in order to better resolve the environmental flow around the storm. Our overall goal was to accurately simulate the time-evolution of Hagibis, starting at the tropical depression stage, continuing through the RI interval, and ending after the completion of the ERC. The objectives of this study are to (i) examine the impacts of horizontal grid spacing on track and intensity forecasts for Typhoon Hagibis; (ii) assess the roles of the finest-resolution moving-nested grid and the fixed outer coarse mesh on the storm's intensification and inner-core structure changes; (iii) evaluate Hagibis's predicted structure during the RI period and ERC w.r.t. the satellite observations from the geostationary satellite Himawari-8 operated by the Japan Meteorological Agency (JMA).

2. Model and experiment description

The COAMPS-TC system, developed by the Naval Research Laboratory (NRL) (Doyle et al. 2014), is used in this study. COAMPS-TC is a regional dynamical tropical cyclone prediction system, run operationally by Fleet Numerical Meteorology and Oceanography Center (FNMOC) for all tropical cyclones worldwide. An operational deterministic version of COAMPS-TC, CTCX,

[2] A registered trademark of the US Naval Research Laboratory.

uses initial and lateral boundary conditions from the GFS global model. CTCX forecasts are routine utilized at operational TC warning centers such as the Joint Typhoon Warning Center and National Hurricane Center. COAMPS-TC is an extensively validated model which produces skillful track and intensity predictions out to 5 days lead time.

For this study, we conducted COAMPS-TC retrospective forecasts of Hagibis based on the version of CTCX run operationally in 2020[3]. Four sensitivity experiments were performed for the 1200 UTC 05 Oct. 2019 forecast of Hagibis, each with a different grid configuration (Table 1). All the experiments used a fixed large outer grid (with the same domain, 8640 x 6480 km) and at least one storm-following moving nested grid. The experiment Q36km3 used the operational grid configuration, consisting of a fixed outer grid at 36 km grid spacing and two storm-following nested grids at 12 km and 4 km grid spacing. Experiment Q36km4 was configured like Q36km3, except it used an additional storm-following nested grid at 1.33 km grid spacing. As shown in Table 1, the addition of the 1.33 km nested grid in Q36km4 is quite expensive, with a computational cost for the Q36km4 run that is 6.5 times that of Q36km3. Experiment Q12km2 utilized a fixed 12 km outer grid and a storm-following 4 km nested grid. Replacing the 36 km outer grid with a 12 km outer grid results in a computational cost for Q12km2 that is 3.6 times that of Q36km3; the finer outer grid is not as computationally expensive as the addition of the 1.33 km nested grid. Finally, experiment Q12km3 was configured like Q12km2, except it used an additional storm-following nested grid at 1.33 km. The initial locations of the storm-following moving nested grids in each experiment are shown as the red boxes in each panel in Fig. 2, respectively. Note that the nested grids are the same size in each experiment; a 12-km nested grid is 1800 x 1800 km (151 x 151 grid points), a 4-km nested grid is 900 x 900 km (226 x 226 grid points), and a 1.33 km nested grid is 320 x 320 km (241 x 241 grid points). Ideally the 1.33 km nested grid would be larger, such that it could encompasses more of the spiral rainband structure in the outer part of the vortex. However the computational expense of a larger 1.33 km grid is prohibitive, viewed from the perspective of what is plausible for operational implementation, so we designed the aforementioned 1.33 km nested grid size in order to focus computational resources on simulation of the inner core region.

[3] Note that the real-time CTCX forecast of Hagibis displayed in Fig. 1 was produced using the 2019 version of the model, which was running operationally at the time. We used the most up-to-date version of COAMPS-TC for our sensitivity experiments.

Other than the grid configuration, aspects of the model set-up are held unchanged among these experiments. The vertical domain consists of 40 sigma-z levels, extending from 10 m above the surface to a model top at approximately 32 km. The initial and boundary conditions are from the GFS 0.25 degree grid analysis and forecast. The physics packages, containing a number of options specialized for tropical cyclone prediction, are as implemented in the 2020 operational version of CTCX. The Kain-Fritsch cumulus parameterization is used for grid spacing at 9-km or larger and a modified bulk microphysics parameterization based on Rutledge and Hobbs (1984) is applied in all domains. The planetary boundary layer turbulent mixing scheme is based on a modified 1.5 order Mellor-Yamada scheme (Mellor and Yamada 1983). A mixing length formulation following Bougeault and Lacarrère (1989), a dissipative heating parameterization (Jin et al. 2007), and the Fu-Liou radiation scheme (Fu and Liou 1993; Liu et al. 2009) are used. The roughness length for momentum is modified to allow the momentum exchange coefficient to level off at wind speeds greater than 25 m s^{-1}, which is based on observations and theory from Donelan et al. (2004), and then the drag decreases with increasing intensity beyond ~30 m s^{-1} (Soloviev et al. 2014). The Geophysical Fluid Dynamics Laboratory (GFDL) tracker (Marchok 2002) is used to determine the storm track and intensity.

3. Initial conditions and COAMPS-TC track & intensity forecasts

Figure 2 shows the large-scale environment at the COAMPS-TC forecast initial time of 1200 UTC 5 Oct. 2019, when Hagibis (tropical depression 20W at the time) was located northwest of the Marshall Islands in the Western North Pacific Ocean. The storm had an intense core of 850-hPa relative vorticity with a maximum of 2×10^{-4} s^{-1} and upper-level diffluence at 200 hPa (Fig. 2a). Two subtropical high centers, one stronger to the northeast of the system and the other weaker to the northwest, are the dominant forcing for the steering flow (Fig. 2b). Vertical wind shear between 850 and 200 hPa is weak (~5 m s^{-1}) near the storm center with the MSLP at 1004 hPa (Fig. 2c). The storm developed in a moist environment, with the 850 hPa relative humidity over 90% within the inner core of the storm (Fig. 2d).

Figure 3 shows the distribution of SST (from the GFS analysis at 1200 UTC 5 Oct. 2019), overlaid with the JTWC best track and the 5-day track forecasts from the four experiments. The SST along the forecast tracks is in the range of 28.5 to 30^{o}C. The best track is located south or west of the forecast tracks, and the SST along the best track is ~ 0.5^{o}C higher in some areas than those along the forecast tracks. Nonetheless the warm SSTs along the forecast track along with abundant low-level moisture, low-level vorticity, and upper-level diffluence over the formative TC at the forecast initial time, all provide a favorable situation for TC RI, consistent with previous studies on the ideal environmental conditions for TC intensification and RI (Merrill 1988; Kaplan et al. 2010).

The COAMPS-TC forecast positions in Fig. 3 match the best track well for the first 12 hours. Subsequently the forecast storm positions, which are very similar amongst the experiments from 12 to 84 h, diverge about 100-150 km to the right of the best track. The forecast position errors from 84 to 120-h remain smaller than 200 km for all the experiments, with the lowest errors from Q36km4 and the highest errors from Q12km2. Overall the tracks from four experiments compare with the best track reasonably well.

Figure 4a is a comparison of the MWS from the four COAMPS-TC experiments with the best track. The four experiments substantially intensify the storm during the first 24 h of the forecast, with all but the Q36km4 experiment exceeding the observed 30 kt (rapid) increase in intensity during that interval. For 24 to 48 h lead time, the MWS from Q36km3, Q36km4 and Q12km3 increases from 66 -106 kt, 54 - 109 kt, and 65 - 131 kt respectively. These rates of intensification (40 kt / 24 h in Q36km3, 55 kt / 24 in Q36km4, 66 kt / 24 h in Q12km3) are all far above the 30 kt / 24 h threshold for RI, but still are well below the 100 kt / 24 h intensification rate for the observed storm. Note that Q12km2 behaves differently from the other three experiments in the 24 – 48 h interval, with a relatively small increase in intensity. However, like the other experiments Q12km2 reaches peak intensity at 60 h lead time, 12 h later compared to the time of the best track peak intensity. In terms of peak intensity, Q12km3 has the highest value of MWS amongst the experiments, at 141 kt (Category 5) compared to 160 kt in the best track. Thus Q12km3 has the fastest intensification rate and the highest peak intensity amongst the four experiments.

Figure 4b presents the comparison of the MSLP from the four COAMPS-TC experiments with the best track. The MSLP decreases during 24-48 h from the Q36km3, Q36km4, and Q12km2 experiments are much smaller than the corresponding MSLP decrease seen in the best track. The MSLP forecast from Q12km3 is noticeably different from the other experiments, with a faster rate of decrease (76 hPa drop in 24 – 60 h interval) and a lower minimum value (896 hPa). However, relative to Q12km3 the best track shows an even faster rate of decrease in MSLP (98 hPa drop in 24-48 h interval) and lower minimum value (890 hPa).

4. Rapid intensification and structure change

a. Observed evolution of storm intensity and structure

Figure 5 shows 10.4 µm wavelength infrared channel geostationary satellite imagery of Typhoon Hagibis from Himawari-8, starting at 0000 UTC 6 Oct. 2019 and ending three days later at 0000 UTC 9 Oct. 2019. At 0000 UTC 6 Oct. 2019 (Fig. 5a), Hagibis was a 45 kt (23 m s^{-1}) tropical storm according to the JTWC best track. Over the next 36 h the storm rapidly intensified into a 160 kt (82 m s^{-1}) super typhoon. Figure 5b shows development of very cold cloud tops (< -80°C, yellow shading) near the center by 1200 UTC 6 Oct. 2019, and by 0000 UTC 7 Oct. 2019 (see Fig. 5c) a small eye was evident. This small eye, surrounded by very cold cloud tops, continued to be present in the infrared imagery through 1800 UTC Oct. 7 2019 (see Fig. 5e), including the time of peak intensity at 1200 UTC Oct. 7 (see Fig. 5d). Note that the JTWC best track specifies the radius of maximum winds as 5 n mi (9 km) during the 0000 UTC 7 Oct. 2019 to 1200 UTC 7 Oct. 2019 period. Fast development of strong convection can also be seen in the outer rainband to the west and southwest of the storm during this RI period.

During the 30-h period subsequent to 1800 UTC Oct. 7 2019, the infrared imagery shows a major structural reorganization. The small eye became less well-defined during the 0000 UTC 8 Oct. 2019 (see Fig. 5f) through 0600 UTC 8 Oct. 2019 (see Fig. 5g) time period, and the JTWC best track analyzes the storm to have weakened to a local minimum in intensity (120 kt, 62 m s^{-1}) at 0600 UTC 8 Oct. 2019. By 1200 UTC 8 Oct. 2019 (see Fig. 5h), it can be inferred that a secondary eyewall has formed with a ring of very cold cloud tops surrounding the remnants of the original small-radius eyewall. Finally by 0000 UTC 9 Oct. 2019 (see Fig. 5i) the original eyewall has dissipated with the secondary eyewall now taking over as the primary eyewall, completing an ERC. At 0000 UTC 9 Oct. 2019 the radius of maximum winds is 15 n mi (28 km) and the intensity has increased back to 145 kt (75 m s^{-1}), according to the JTWC best track.

b. COAMPS-TC simulation of rapid intensification

Recall that the predicted rate of intensification and peak intensity in COAMPS-TC experiment Q12km3 are markedly different from those of the other three COAMPS-TC experiments. In conjunction with these intensity differences there are also major inner-core structural differences between Q12km3 and the other three experiments, which we will describe in detail here.

Figure 6 shows the COAMPS-TC 10-m winds (color shading and streamlines) and sea-level pressure (black contours) in the region encompassing the TC core at the 72 h lead time for each of the four experiments. By 72-h, RI has ended in all COAMPS-TC experiments such that the storm is near its forecast peak intensity. The two experiments with 4 km grid spacing on the innermost nest, Q36km3 and Q12km2, show an intense, but fairly broad inner core wind field, with a radius of maximum winds (RMW) of 42 km in Q36km3 (and even larger in Q12km2). Both experiments with 1.33 km grid spacing on the innermost nest (Q36km4 and Q12km3) have smaller RMWs. The RMW in Q36km4 is 22 km, considerably smaller than that of Q36km3, but otherwise the appearance of the vortex wind field at the 10-m level is largely similar between Q36km4 and Q36km3 (though the maximum wind speed is 5 ms^{-1} higher in Q36km3). However, the nature of the vortex wind field at 10-m in Q12km3 is quite different from Q36km3. The vortex in Q12km3 is very small and intense with an RMW of just 12 km, which is close to the JTWC best track RMW estimate of 9 km at the time of the storm's peak intensity. Additionally, in Q12km3 40 m s^{-1} winds only extend to a radius of 25 km; such winds extend between 2 and 3 times as far in Q36km3. These results indicate that the forecast inner core structure is sensitive to model grid spacing in the inner-core region, as we anticipated would be the case. However the inner core structure also appears to be sensitive to the grid spacing of the outer mesh, given that Q36km4 and Q12km3 differ only in grid spacing in that part of the model domain.

Figure 7 shows simulated radar reflectivity (color shading) alongside sea-level pressure (black contours) for the four experiments as in Fig. 6. Here it is clear that convective features with smaller horizontal scales are represented in the experiments with 1.33 km grid spacing on the innermost nest (Q36km4, Q12km3), relative to the experiments with 4 km grid spacing on the innermost nest (Q36km3, Q12km2). This is also true of the 10-m wind fields shown in Fig. 6, though it is not quite as visually striking in the winds as it is for the simulated radar reflectivity. Comparing Figs. 6 and 7, it can be seen that high reflectivity is coincident with the strongest 10-m winds; this is the eyewall of the storm. The eyewall convection is particular intense and axisymmetric in Q12km3, in comparison with the other experiments. The reflectivity for Q12km3 also appears to have a secondary maximum at larger radius separated from the eyewall by a low-reflectivity "moat" (the narrow region outside the eyewall but inside the outer convective bands), features which are not readily apparent in the other three experiments (see Sec. 5c for discussion of SEF).

Figure 8 shows radius-time plots of the azimuthally-averaged 10-m wind speed (contours) and surface latent heat flux (color shading), along with the RMW (green line) during 24 to 120 h lead time. For brevity only the Q36km3 (Fig. 8a), Q36km4 (Fig. 8b), and Q12km3 (Fig. 8c) experiments are shown (same for the forthcoming Figs. 9, 10, and 11) as of the four experiments, these three have the most realistic depiction of the storm's intensity and structural evolution. Here we are particularly interested in the role of inner-core grid resolution on the time-evolution of the RMW through the period of forecast RI and ending at the 72 h lead time (shown in Figs. 6 and 7). In the three COAMPS-TC experiments shown in Fig. 8, the RMW contracts as the storm intensifies at early lead times. In Q36km3, contraction of the RMW stops at 36 h lead time. Then the RMW gradually migrates outward through the end of the forecast, including the latter part of RI phase of the forecast between 36 h and 60 h. In Q36km4, contraction of the RMW ends at 42 h and then is roughly constant through 72 h as the forecast storm completes RI. For Q12km3, the period of RMW contraction lasts through 60 h lead time, accompanying the entire period of RI. The RMW then remains constant through 72 h lead time. The Q12km3 experiment did best in terms of contracting the RMW to near the JTWC best track value of 9 km, but the storm was observed to attain this RMW value by 36 h into the forecast, whereas the RMW contraction took about 24 h longer in Q12km3. In summary, the two experiments with 1.33 km grid spacing in the inner core region (Q36km4, Q12km3) develop a more compact RMW than Q36km3 (with 4 km grid spacing in the inner-core region). But Q12km3, with 12 km grid spacing on the outermost fixed mesh, shows more RMW contraction and intensification than Q36km4 (36 km grid spacing on the outermost fixed mesh).

To be clear, we are not asserting that RMW contraction is governing the intensification rate either in our simulations or in reality. Hagibis' observed intensification and RMW contraction (as seen in the JTWC best track) is broadly consistent with Stern et al. (2015), who based on idealized simulations and observations of real storms concluded that "most [RMW] contraction occurs prior to most intensification". Hagibis intensified from 30 kt to 105 kt accompanied by a decrease in RMW from 30 n mi to 5 n mi; subsequent intensification to 160 kt occurred with the RMW constant at 5 n mi. The Q36km4 and Q12km3 simulations, both which utilize 1.33 km grid spacing in the inner core, are most consistent with the Hagibis observations in terms of the timing of intensification/RMW contraction. On the other hand, the Q36km3 simulation *increased* the

RMW during the latter part of its simulated RI, which is not consistent with the Hagibis best track observations or other observed storms described in Stern et al. (2015).

The surface latent heat flux plays an important role in the RI, in the sense that surface fluxes are coupled with intensification of the vortex and its surface wind field. The azimuthally-averaged surface latent heat flux results in Fig. 8 show that the strongest azimuthally-averaged 10-m winds are coincident with the largest values of azimuthally-averaged latent heat flux. For a given 10-m wind speed, the latent heat flux tends to be larger earlier in the forecast when the storm was located over relatively warm SSTs, contributing to the storm's exceptionally fast intensification rate. The surface latent flux from Q12km3, which is much larger than those in Q36km3 and Q36km4, is associated with the stronger RI in that experiment.

c. COAMPS-TC simulation of secondary eyewall formation

So far we have discussed the structural evolution of the COAMPS-TC predicted storm during the RI phase up through 72 h lead time. Beyond 72 h, Fig. 8 shows continued differences in the time-evolution of the azimuthally-averaged 10-m winds among the Q36km3, Q36km4, and Q12km3 experiments. In particular, the RMW for experiments Q36km4 and Q12km3 (both with 1.33 km grid spacing in the inner-core region) is represented discontinuously in Fig. 8, with a jump to larger radius after 72 h. We will show that the TC in experiments Q36km4 and Q12km3 undergoes SEF, with Q12km3 clearly completing an ERC. In contrast, the TC in experiment Q36km3 (with 4 km grid spacing in the inner-core region) does not undergo SEF or an ERC.

Before examining the results it is worth noting that the large-scale environment around Hagibis leading up to the ERC in the simulations is generally consistent with those of real typhoons that form a concentric eyewall and go on to complete an ERC (Zhu and Yu, 2019). At 72 h in the simulations, Hagibis is near 19°N (see Fig. 3), and leading up to that time it is far enough south to be substantially displaced from a broad subtropical 500-hPa ridge predicted to be centered north of the storm and extending along an east-west axis about 25°N. The position of the storm w.r.t. the 500-hPa subtropical ridge appears more like the quiescent 500-hPa composite environment shown by Zhu and Yu (2019; see their Fig. 13) for typhoons that completed an ERC rather than their 500-hPa composite environment for typhoons that form a concentric eyewall and subsequently do not complete an ERC.

Radius-height plots in Figs. 9 and 10 display the time-evolution of the azimuthal mean structure of the TC vortex core between 60 h and 84 h lead time, when the predicted storm is near peak intensity in all four experiments (see Fig. 4a). In Figs. 9 and 10, the azimuthally averaged radius-height plots from experiments (a-c) Q36km3, (d-f) Q36km4, (g-i) Q12km3 are displayed at 60 h, 72 h, and 84 h respectively.

Figure 9 shows the tangential (black contours) and radial (color shading) components of the azimuthal mean wind. In Q36km3 a slow outward expansion of the low-level tangential winds can be seen, with the RMW at 1 km altitude increasing from about 40 km at 60 h lead time to about 55 km at 84 h lead time. The results for experiment Q12km3 show a rather different evolution of the inner core wind field. The 1-km altitude RMW is approximately 18 km for all three lead time shown. However, at 84 h a secondary maximum in the 1-km azimuthal mean tangential wind profile develops at about 65 km radius. Finally, the Q36km4 experiment shows an evolution of the tangential winds that encompasses both an outward expansion of the RMW (as seen in Q36km3) and formation of a secondary maximum in the azimuthal mean tangential wind profile (as seen in Q12km3).

It is important to note the nature of the radial profile of the low-level tangential winds at 60 h and 72 h in Fig. 9. Beyond 40 km radius, Q12km3 shows a much more gradual decrease in tangential wind speed with radius than Q36km3 and Q36km4. A broad area of relatively constant 10-m winds located outside the inner core in the Q12km3 experiment at 72 h can also be seen in Fig. 6d, differing markedly from the 72 h wind fields from Q36km3 (Fig. 6a) and Q36km4 (Fig. 6b). This broadening of the wind field outside the inner core seen in Q12km3 is a precursor to SEF, following the sequence described by Huang et al. (2012). The state of the radial profile of the tangential winds at the end of the RI period appears to be a key factor governing which COAMPS-TC simulations undergo SEF and which do not.

Another noteworthy aspect of the simulations represented in Fig. 9 is the depth and structure of the azimuthal mean radial inflow layer. The Q12km3 experiment has a thinner layer of radial inflow relative to Q36km3 and Q36km4. The experiments all use identical vertical levels, so vertical resolution is not responsible for the aforementioned differences in the depth of the inflow layer. It is likely that the overall vortex structure enabled by 1.33 km horizontal grid spacing (i.e. intense, small inner core) in Q12km3 is associated with the relatively thin radial inflow layer in that experiment.

Figure 10 shows azimuthal mean tangential winds (black contours), diabatic heating rate (color shading), and vertical velocity (green contours). The latter two quantities indicate the presence of convection. Note that whereas Fig. 9 extends from the surface to 5 km altitude, Fig. 10 extends to 12 km altitude.

The results for Q36km3 (Figs 10a-c) indicate the outward expansion of the RMW in that experiment is accompanied by the outward expansion of the eyewall convection, with a radially thick area of diabatic heating / ascent located near or just inward of the RMW. Again the results in the bottom row of Fig. 10, for experiment Q12km3, differ markedly from Q36km3. A relatively narrow area of diabatic heating / ascent is located near or just inward of the small RMW at all lead times during 60-84 h. At 84 h, there is a second area of diabatic heating / ascent associated with the secondary maximum in the tangential wind profile. With a local maximum in tangential winds and convective activity, this constitutes a secondary eyewall. As for Q36km4 (Figs. 10d-f), the diabatic heating / ascent indicates that a secondary convective maximum (in addition to the maximum associated with the RMW) has formed by 72 h and is the dominant convective feature by 84 h. Overall, considering both the evolution of the tangential winds and convection, it does appear the simulated storm in Q36km4 undergoes a SEF, though it is not as distinct as in Q12km3.

To further examine the time-evolution of the azimuthal mean tangential wind field (at 1 km altitude) and diabatic heating / ascent (at 6.5 km altitude), radius-time plots are shown for experiments Q36km3 (Fig. 11a), Q36km4 (Fig. 11b), and Q12km3 (Fig. 11c). In Q36km3, there is no indication of SEF in the latter half of the forecast. In Q12km3, a secondary eyewall is evident by 84 h lead time. At the same time, the primary eyewall at small radius is weakening. Over the next 12 h the secondary eyewall intensifies and contracts, while the small-radius eyewall continues weakening. After 96 h, the ERC is completed, as the small-radius eyewall completely dissipates and the secondary eyewall takes over as the primary eyewall. The ERC in the Q12km3 simulation is qualitatively similar to what was observed in the actual storm. Finally, as discussed in the context of Figs. 9 and 10, the evolution of the Q36km4 forecast contains features seen in both Q36km3 and Q12km3. In the latter half of the forecast, the RMW migrates outward in a mostly similar fashion to Q36km3. However unlike Q36km3 there is a subtle SEF around 72 h lead time, when there is briefly an inner and outer maxima in the 1-km azimuthally averaged tangential winds, each associated with local maxima in the diabatic heating / ascent. This is not a clear ERC as seen in Q12km3, but instead seemingly a SEF superimposed on top of the gradual expansion of the RMW. In summary, the results demonstrate that the higher resolutions of the outermost fixed mesh and the innermost moving nest (less than 2 km) are important to both RI and TC structure variations. This is presumably due to the increased capability of resolving convections over a wider area by the higher grid spacing in the outer fixed mesh of Q12km3, in addition to its very high resolution in the inner-core region.

d. Influence of outer grid resolution on the storm's structural evolution

There are substantial differences in simulation of storm intensity and storm structure between the Q36km4 and Q12km3 experiments, as detailed in this section as well as Sec. 3. These two experiments differ only in the grid spacing utilized on the fixed outer model grid. Outside of a 1800 x 1800 km storm-centered box, Q36km4 uses 36 km grid spacing while Q12km3 uses 12 km grid spacing. Inside the 1800 x 1800 km storm-centered box, the grid spacing used by the two experiments is identical. Differences between the two experiments must be rooted in differences in simulation of the storm environment outside the 1800 x 1800 km box (note the same is true for the Q36km3 and Q12km2 simulations).

Comparing the two simulations using 36 km grid spacing on the outer grid (Q36km3 and Q36km4) and the two simulations using 12 km grid spacing on the outer grid (Q12km2, Q12km3), we found consistent differences in environmental moisture that influence the nature of the storm's distribution of moisture and convection. Figure 12a-b shows total precipitable water (TPW) and surface-to-850 hPa averaged winds from the Q36km4 and Q12km3 experiments at the 24 h lead time; Figure 12c shows the TPW difference field (Q12km3 – Q36km4) at 24 h and the Q12km3 surface-to-850 hPa averaged winds (for context). For simplicity, the Q36km3 and Q12km2 experiments are not included in Fig. 12, as Q36km3 is similar to Q36km4 and Q12km2 is similar to Q12km3 regarding environmental moisture. At 24 h in Q12km3, there is higher TPW air wrapping around the eastern, northern, and western portions of the storm relative to that seen in Q36km4 (note also the less prominent dry slot in the SE quadrant outside the TC core in the Q12km3 run). The moist air wrapping cyclonically around the storm appears to originate well to the south of the TC in the deep tropics, outside the 1800 x 1800 km storm-centered box where there are differences in grid spacing between the Q36km4 experiment and the Q12km3 experiments.

Figure 12d-f are similar to Fig. 12a-c, but show 850-hPa relative humidity and 850-hPa wind. Here, there appear to be systematic differences in the model state at 24 h lead time. In particular, 850-hPa humidity is higher in the southernmost portion of Fig. 12e (Q12km3) with respect to Fig. 12d (Q36km4). The model dynamics and physical parameterizations (in particular deep cumulus parameterization) operating at 12-km grid spacing vs. 36-km grid spacing lead to subtle but systematic differences in the simulation of moist air flowing from the south and wrapping cyclonically around the storm.

The aforementioned differences in moisture wrapping into the storm between the Q36km4 and Q12km3 experiments have implications for the convective structure of the storm, as shown by the composite simulated reflectivity fields in Fig. 13. At 24 h, and especially 48 h, there is greater reflectivity coverage in the SE quadrant of the storm in the Q12km2 and Q12km3 experiments w.r.t. Q36km4, indicating more saturated conditions there and less influence of dry air wrapping around the inner core of the storm from the SW quadrant to the SE quadrant. Better protection of the TC inner core from the dry air in the Q12km3 run relative to experiment Q36km4 likely helped promote the greater intensification of the storm in Q12km3. Finally, at 72 h Fig.13 shows that the Q12km2 and Q12km3 runs have reflectivity coverage further from the center than in Q36km4, in all directions except to the west. The larger moist and convectively active region encompassing the storm in Q12km2 and Q12km3 w.r.t. Q36km4 is more conducive to SEF and subsequent ERC, and is likely part of the reason why Q12km3 has a very well-defined SEF and ERC while Q36km4 only has a subtle SEF superimposed on top of an expanding RMW.

e. Comparison of simulated TC structure variation with satellite imagery

To summarize the structure evolution of Hagibis in experiment Q12km3, Fig. 14 shows the simulated radar reflectivity starting at 0000 UTC 6 Oct. 2019 and ending at 0000 UTC 10 Oct. 2019. This time interval covers the period of RI as well as the ERC in experiment Q12km3. Hagibis is still relatively weak at 12-h lead time in the forecast, with MWS at 49 kt and MSLP at 988 hPa. Convective bands are primarily found in the south and southwestern quadrants (Fig. 14a). From 24 to 36 h lead time (Figs. 14b,c), an eyewall forms as the inner core becomes better organized and Hagibis rapidly intensifies from Category 1 to 3, with a drop in MSLP from 975 to 955 hPa. During this time, the outer convective bands in the simulation are mostly in the southwest quadrant, similar to the convective distribution shown in the satellite imagery (Fig. 5b,c). From 36 to 48 h, Hagibis continues to rapidly intensify in the Q12km3 experiment, attaining an MSLP of 918 hPa and MWS of 131 kt at 48h (Fig. 14d). At 48 h, the simulation shows a small-scale inner core with a clear eye surrounded by a high-reflectivity eyewall. The forecast storm reaches its peak intensity at 60 h with an MSLP of 899 hPa and MWS of 141 kt, still accompanied by the small clear eye and high-reflectivity eyewall.

By the 72 h lead time (Fig. 14f), Hagibis starts to weaken with an MSLP 900 hPa and MWS of 136 kt, and the formative secondary eyewall is apparent in the simulated radar reflectivity, which is similar to the satellite observation shown in Fig. 5f. The inner eyewall weakens as the outer eyewall contracts to a smaller radius at 84 h (Fig. 14g), which is similar to Fig. 5g. Hagibis continues to weaken in the simulation with an MSLP of 915 hPa and MWS of 99 kt and its inner eyewall starts to dissipate at 96 h (Fig. 14h), which is similar to Fig. 5h. The forecast storm weakens further and has an MSLP of 929 hPa and MWS of 99 kt at 108 h, and its inner eyewall dissipates almost completely (Fig. 14i).

The storm structure variations seen from the simulated radar reflectivity from experiment Q12km3 during the RI and ERC bear considerable resemblance to the observed satellite images from Himawari-8. These results suggest that the higher horizontal resolution enabled by the grid settings of the Q12km3 experiment are very important to the prediction of the structural evolution of Typhoon Hagibis.

5. Summary and Conclusions

Super Typhoon Hagibis was a large and very intense storm that had significant societal impacts in Japan. Our results suggest that the large-scale environment present just after genesis, particularly the upper-level divergence, lower-level convergence, weak vertical wind shear, ample low-level moisture supply, and warm SSTs set the stage for Hagibis's RI. Hagibis went on to form a very small inner core (9 km RMW) and intensified extremely rapidly to a 160 kt (82 m s^{-1}) peak intensity. The storm then went through an ERC that resulted in a slightly weaker storm (145 k, 75 m s^{-1}), but with a larger inner core (15 n mi, 28 km RMW). It is very challenging to simulate this type of storm evolution (RI followed by an ERC) with a regional dynamical tropical cyclone prediction model, like the COAMPS-TC model employed here.

We demonstrated that the operational configuration of the COAMPS-TC model as of 2020 (i.e. experiment Q36km3), using 36 km grid spacing on the fixed outer grid and two storm-following inner grids at 12 km and 4 km grid spacing, is capable of rapidly intensifying Hagibis from a tropical depression to a strong typhoon. However, this configuration does not intensify the storm fast enough, with the simulated storm too weak (by 55 kt) at the time of the observed peak intensity. The Q36km3 configuration also does not contract the RMW to as small of a value as seen in reality and does not go through an ERC. For much of the simulated RI in Q36km3, the RMW expands and continues expanding through the end of the forecast. With 4-km grid spacing on the innermost nest, the Q36km3 configuration does not have high enough horizontal resolution to simulate an extremely intense storm with a ~10 km RMW and appears to be unable to convincingly simulate an ERC.

Here we have shown results for three sensitivity experiments, which differed from Q36km3 only in terms of horizontal grid spacing. The Q12km2 experiment, which used a 12-km fixed outer grid and one storm-following 4-km grid, simulated Hagibis in a largely similar manner to Q36km3. The Q36km4 experiment, configured the same as Q36km3 except for the addition of a 1.33-km storm-following nest covering the inner core region, produced a considerably smaller RMW than Q36km3 and showed evidence of SEF. However, despite the more realistic simulation of storm structure relative to Q36km3, Q36km4 produced a very similar intensity forecast. The final experiment, Q12km3, which used a 12-km fixed outer grid with 4-km and 1.33-km storm-following grids, produced a forecast of intensity and storm structure that was clearly superior to the other three experiments. Q12km3 intensified the storm more rapidly than the other experiments and achieved a higher peak intensity. The intensification of the storm was accompanied by a contraction of the RMW to near the unusually small value observed for Hagibis. And after RI, the Q12km3 storm underwent an ERC qualitatively similar to that of the observed storm. The Q12km3 forecast was by no mean flawless. The TC in Q12km3 reached peak intensity 12 h too late (and 19 kt too weak), and completed the ERC about 24 h too late. It also weakened the storm too much during the ERC. Nonetheless, in terms of both intensity and structure prediction, Q12km3 was by far the best of the four COAMPS-TC simulations.

The results of experiments Q36km3 and Q12km3 underscore the substantial sensitivity of the COAMPS-TC intensity and structure forecast for Hagibis to the grid spacing utilized for the inner-core region of the storm (4 km for Q36km3 and 1.33 km for Q12km3). The improved horizontal resolution for the storm inner core accompanying the 1.33 km grid spacing enables the model to realistically simulate (1) an explosive RI, with (2) an unusually small inner core, followed by (3) an ERC. None of these three features were realistically simulated in the Q36km3 experiment, representing the operational model configuration. This is a key outcome of our Hagibis case study. However given the aforementioned context, the results of the Q36km4 experiment (which uses 1.33 km grid spacing in the inner core region) are curious in the sense that they are not more similar to Q12km3. The only configuration difference between Q36km4 and Q12km3 is that outside the 1800 x 1800 km region centered on the storm, Q36km4 utilized 36 km grid spacing and Q12km3 utilized 12 km grid spacing. Nonetheless, this configuration difference does appear to be relevant to the simulated evolution of the storm. We showed that there are subtle but systematic differences between Q36km4 and Q12km3 in the representation of the moist flow originating from the deep tropics, outside the 1800 x 1800 km box, and wrapping cyclonically into the storm. The implications for the vortex are that in Q12km3 w.r.t. Q36km4, there is a less-pronounced dry slot wrapping around the south side of the inner core during the period of RI, and a larger moist and convectively active region associated with the storm at the time of SEF.

In summary, we use the Hagibis case study to gain a better understanding of the relationship of RI and SEF/ERC to horizontal grid spacing. We found that the storm can develop to Category 4 with the finest grid spacing at 4-km, though with a much slower intensification rate than observed and an inner core that is too big. That means that simulation at 4-km grid spacing is not sufficient to resolve the small inner core at a horizontal scale of ~10 km. The SEF/ERC occurs only when the inner core is quite small, which is only possible with the grid spacing at 1.33 km. Therefore the 4-km grid spacing is capable of producing an RI, but it is not enough for the subsequent ERC. The 1.33 km grid spacing is a necessary condition to resolve a small inner core to set the stage for SEF/ERC, but it is not sufficient condition for happening of SEF/ERC.

As mentioned in Section 1, COAMPS-TC is an operational model, run in real-time with computational resource and timing constraints. Relative to the operational grid configuration (represented by experiment Q36km3), it would take a very large investment in computational resources to introduce a 1.33 km storm-following nest for the inner-core region of the storm. Even just changing the fixed outer grid from 36 to 12 km would necessitate a substantial increase in the computational resources allocated to the model. Further study of the sensitivity of COAMPS-TC model forecasts to horizontal grid spacing, in the context of a large sample of TC cases, is needed to better understand the impacts of these grid changes on intensity and structure predictions. It is of particular interest to better characterize the importance of grid spacing outside of the storm on inner-core structural evolution, given the sensitivity of the Hagibis simulations to differences in grid spacing well away from the TC itself. This is a subject for future work, motivated by the results here indicating the promise of higher model resolution to achieve realistic simulations of a very challenging forecast case such as Super Typhoon Hagibis.

Data Availability Statement: The model forecast datasets generated and analyzed in this study, which are very large in size, are not publicly available due to United States Department of Defense (DoD) policies. However, they are available from the corresponding author with a reasonable request, subject to the permissions from our funding agencies and DoD approval for public release.

Acknowledgments: Thanks for the anonymous reviewers' helpful suggestions for further improving this manuscript. This research is supported by the Chief of Naval Research through the Office of Naval Research High-resolution COAMPS-TC Prediction of RI and SEF, 0602435N and COAMPS-TC RTP, 0603207N. We acknowledge computational support from a grant of High Performance Computing (HPC) time from the Navy Defense Resource Center (DSRC) at Stennis, MS. COAMPS-TC is a registered trademark of the Naval Research Laboratory.

References

Abarca, S. F., and M. T. Montgomery, 2013: Essential dynamics of secondary eyewall formation. *J. Atmos. Sci.*, **70**, 3216–3230.

——, and ——, 2014: Departures from axisymmetric balance dynamics during secondary eyewall formation. *J. Atmos. Sci.*, **71**, 3723–3738.

——, and ——, 2015: Are eyewall replacement cycles governed largely by axisymmetric balance dynamics? *J. Atmos. Sci.*, **72**, 82–87.

AON, 2020: Weather, climate & catastrophe insight: 2019 annual report. 23 January 2020.

Bougeault, P., and P. Lacarrère, 1989: Parameterization of orography induced turbulence in a meso-beta-scale model. *Mon. Wea. Rev*., **117**, 1872–1890.

Donelan, M. A., B. K. Haus, N. Reul, W. J. Plant, M. Stiassnie, and H. C. Graber, 2004: On the limiting aerodynamic roughness of the ocean in very strong winds. *Geophys. Res. Lett.,* **31,** L18306, doi:10.1029/2004GL019460.

Doyle, J. D., R. Hodur, S. Chen, Y. Jin and J.R. Moskaitis, S. Wang, E. A. Hendricks, H. Jin, and T. Smith, 2014: Tropical cyclone prediction using COAMPS-TC. *Oceanography,* **27,** 104–115.

Emanuel, K. A., 1986: An air-sea interaction theory for tropical cyclones. Part I: Steady-state maintenance. *J. Atmos. Sci.,* **43,** 585–604.

——, 1994: Atmospheric Convection. *Oxford University Press,* 580 pp.

——, 2003: Tropical cyclones. *Annu. Rev. Earth Planet. Sci.*, **31,** 75–104.

Fu, Q., and K. N. Liou, 1993: Parameterization of the radiative properties of cirrus clouds. *J. Atmos.*

Sci., **50,** 2008–2025.

Gopalakrishnan, S. G., M. Frank, X. Zhang and Coauthors, 2011: The experimental HWRF system: A study on the influence of horizontal resolution on the structure and intensity changes in tropical cyclones using an idealized framework. *Mon. Wea. Rev.*, **139**, 1762-1784.

Holiday, C. R., and A. H. Thompson, 1979: Climatological characteristics of rapidly intensifying typhoons. *Mon. Wea. Rev.*, **107**, 2022–1034.

Huang, Y.-H., M. T. Montgomery, and C. C. Wu, 2012: Concentric eyewall formation in Typhoon Sinlaku (2008). Part II: Axisymmetric dynamical processes. *J. Atmos. Sci.*, **69,** 662–674.

Japan Meteorological Agency, 2020: Metrological, earthquake and volcanic activity report, retrieved 20 February 2020.

Jin, H., M. Peng, Y. Jin, J.D. Doyle, 2014: An evaluation of the impact of horizontal resolution on tropical cyclone predictions using COAMPS-TC, *Wea. Forecasting*, **29,** 252–270.

Jin, H., Y. Jin, and J. D. Doyle, 2019: An evaluation of COAMPS-TC real-time forecasts for Super Typhoon Nepartak (2016). *J. Meteor. Soc. Japan*, **97**, 191-203.

Jin, Y., W. T. Thompson, S. Wang, and C.-S. Liou, 2007: A numerical study of the effect of dissipative heating on tropical cyclone intensity. *Wea. Forecasting*, **22,** 950–966.

Kaplan, J., and M. DeMaria, 2003: Large-scale characteristics of rapidly intensifying tropical cyclones in the North Atlantic basin. *Wea. Forecasting*. **18,** 1093–1108.

Kaplan, J., M. DeMaria, and J. A. Knaff, 2010: A revised tropical cyclone rapid intensification index for the Atlantic and eastern North Pacific basins. *Wea. Forecasting*, **25**, 220–241.

Liu, M., J. E. Nachamkin, and D. L. Westphal, 2009: On the improvement of COAMPS weather forecasts using an advanced radiative transfer model. *Wea. Forecasting*, **24**, 286–306.

Marchok, T. P. 2002: How the NCEP tropical cyclone tracker works. Preprints, *25th Conf. Hurr. Trop. Meteor.,* San Deigo, CA, 21–22.

Mellor, G., and T. Yamada, 1983: A hierarchy of turbulence closure models for planetary boundary layers. *J. Atmos. Sci.*, **32**, 1278–1282.

Merrill, R. T., 1988: Environmental influences on hurricane intensification. *J. Atmos. Sci.*, **45**, 1678–1687.

Montgomery, M. T. and R.J. Kallenbach, 1997: A theory for vortex Rossby waves and its application to spiral bands and intensity changes in hurricanes. *Quart. J. Roy. Meteor. Soc.*, **123**, 435-465.

Montgomery, M. T. and R. K. Smith, 2014: Paradigms for tropical-cyclone intensification. *Aust. Meteor. Oceanogr. J.*, **64,** 37–66.

New York Times, 2019: Typhoon Hagibis slams into Japan after landslides, floods and a quake, Oct. 13, 2019.

Rutledge, S. A. and P.V. Hobbs, 1984: The mesoscale and microscale structure and organization of clouds and precipitation in mildlatitude cyclones. XII: A diagnostic modeling study of precipitation development in narrow cold-frontal rainbands. *J. Atmos. Sci.*, **41**, 2949–2972.

Soloviev, A. V., R. Lukas, M. A. Donelan, B. K. Haus, and I. Ginis, 2014: The air-sea interface and surface stress under tropical cyclones. *Sci. Rep.*, **4**, 5306; DOI: 10.1038.

Stern, D.P., J. Vigh, D.S., and F. Zhang, 2015: Revisiting the relationship between eyewall contraction and intensification. *J. Atmos. Sci.*, **72**, 1283-1306.

Wada, A. and J. C.L. Chan, 2021: Increasing TCHP in the western north Pacific and its influence on the intensity of Faxai and Hagibis in 2019. *SOLA*, **17A**, 19-32.

Wang, H., C.C. Wu and Y. Wang, 2016: Secondary eyewall formation in an idealized tropical cyclone simulation: Balanced and Unbalanced dynamics. *J. Atmos. Sci.*, **73**, 3911-3930.

Wu, C.-C., Y.-H., Huang, and G.-Y. Lien, 2012: Concentric eyewall formation in Typhoon Sinlaku (2008). Part I: Assimilation of T-PARC Data Based on the Ensemble Kalman Filter (EnKF). *Mon. Wea. Rev.*, **140,** 506–527.

Zhu, P., 2015: On the mass-flux representation of vertical transport in moist convection. *J. Atmos. Sci.*, **72**, 2011-2019

——, Zhu. Z., Gopalakrishran, S. and coauthors, 2015: Impact of subgrid-scale processes on eyewall replace cycle of tropical cyclones in HWRF system. *Geophys. Res. Lett.*, **42,** 10027-10036.

Zhu, T., D.-L. Zhang and F. Weng, 2004: Numerical simulation of Hurricane Bonnie (1998). Part I: Eyewall evolution and intensity changes. *Mon. Wea. Rev.*, **132**, 225-241.

Zhu, X.-S., and H. Yu, 2019: Environmental influences on the intensity and configuration of tropical cyclone concentric eyewalls in the western north Pacific. *J. Meteor. Soc. Japan*, **97**, 153-173.

Zhu, Z.-D., and P. Zhu, 2014: The role of outer rainband convection in governing the eyewall replacement cycle in numerical simulations of tropical cyclones, *J. Geophys. Res. Atmos.*, **119**, 8049–8072.

Table List

Table 1 Configurations of four sensitivity experiments and their computational costs are listed in the following table. The experiment (EXP, such as Q36km3) names used here indicate the grid spacing of the fixed outermost grid (e.g. 36 km) and the total number of grids (e.g. 3). The first character Q indicates that the quarter degree grid analysis of GFS are used for the initial and boundary conditions.

EXP Name	Outermost Grid Spacing	No. of Nest	Dimensions for Moving Nests	Innermost Grid Spacing	Ratio of Cost
Q36km3	36 km	3	151x151, 226x226	4 km	1.0
Q36km4	36 km	4	151x151, 226x226, 241x241	1.33 km	6.5
Q12km2	12 km	2	226x226	4 km	3.6
Q12km3	12 km	3	226x226, 241x241	1.33 km	58.9

Figures

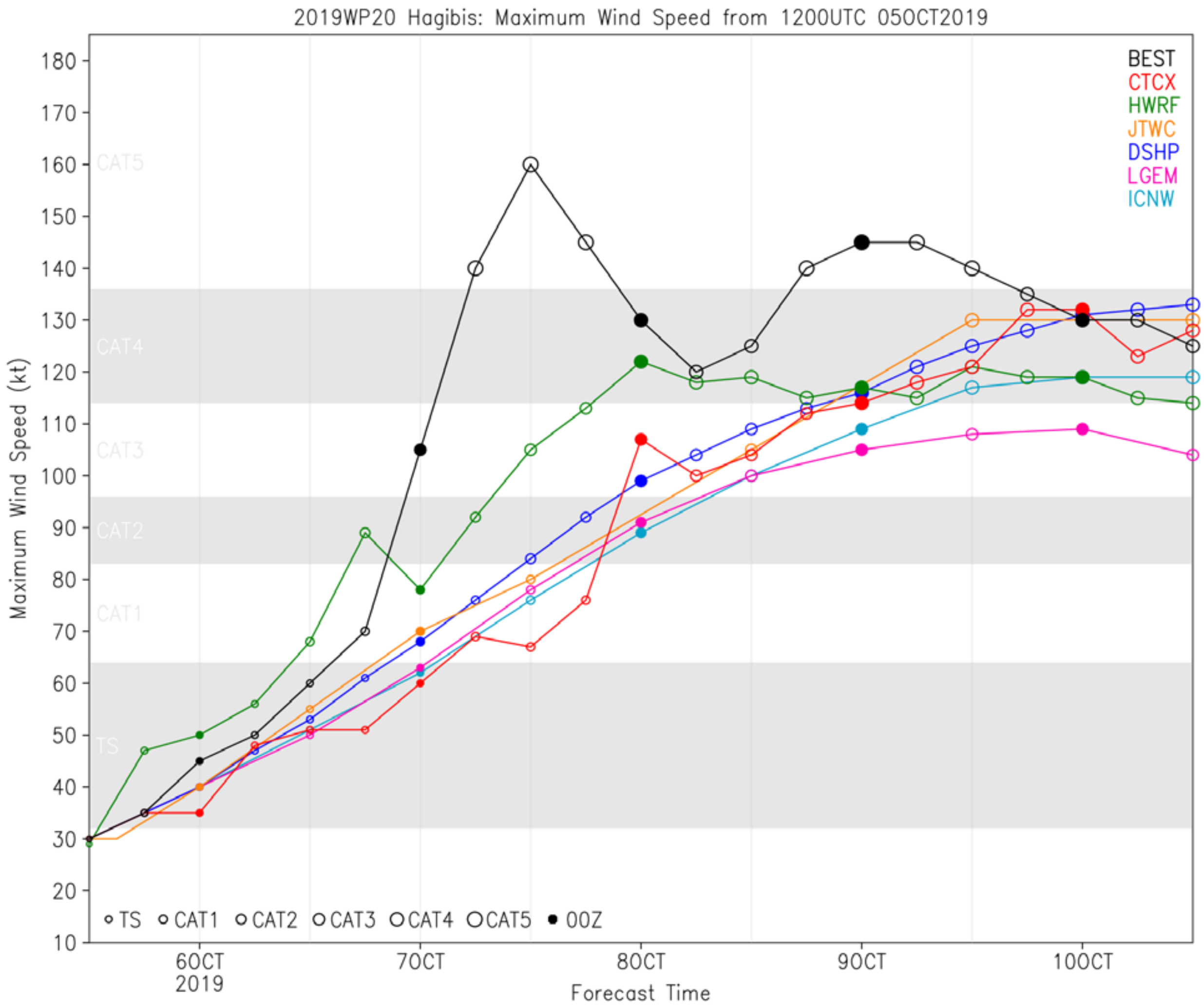

Fig. 1. Comparison of real-time multi-model 5-day intensity forecasts for Typhoon Hagibis (2019) starting at 1200 UTC 5 Oct. 2019 with the best-track (black). Operational forecasts failed to predict it as a category 5 storm and it is still a challenge to predict the steep RI rates observed. The color lines are shown as following: the CTCX (red) is for COAMPS-TC; the HWRF (green) is for the NOAA Hurricane WRF model; the JTWC (orange) is for the official forecast from the Joint Typhoon Warning Center (JTWC); the DSHP (blue) is for Decay Statistical Hurricane Intensity Prediction Scheme (also known as D-SHIPS), a version of SHIPS that can predict weakening due to land interaction; the LGEM (pink) is for SHIPS Logistic Growth Equation forecast Model; and the ICNW (light blue) is for the operational JTWC tropical cyclone intensity consensus. DSHP and LGEM are statistical intensity forecast models, and the ICNW consensus is the average intensity forecast considering a set of models.

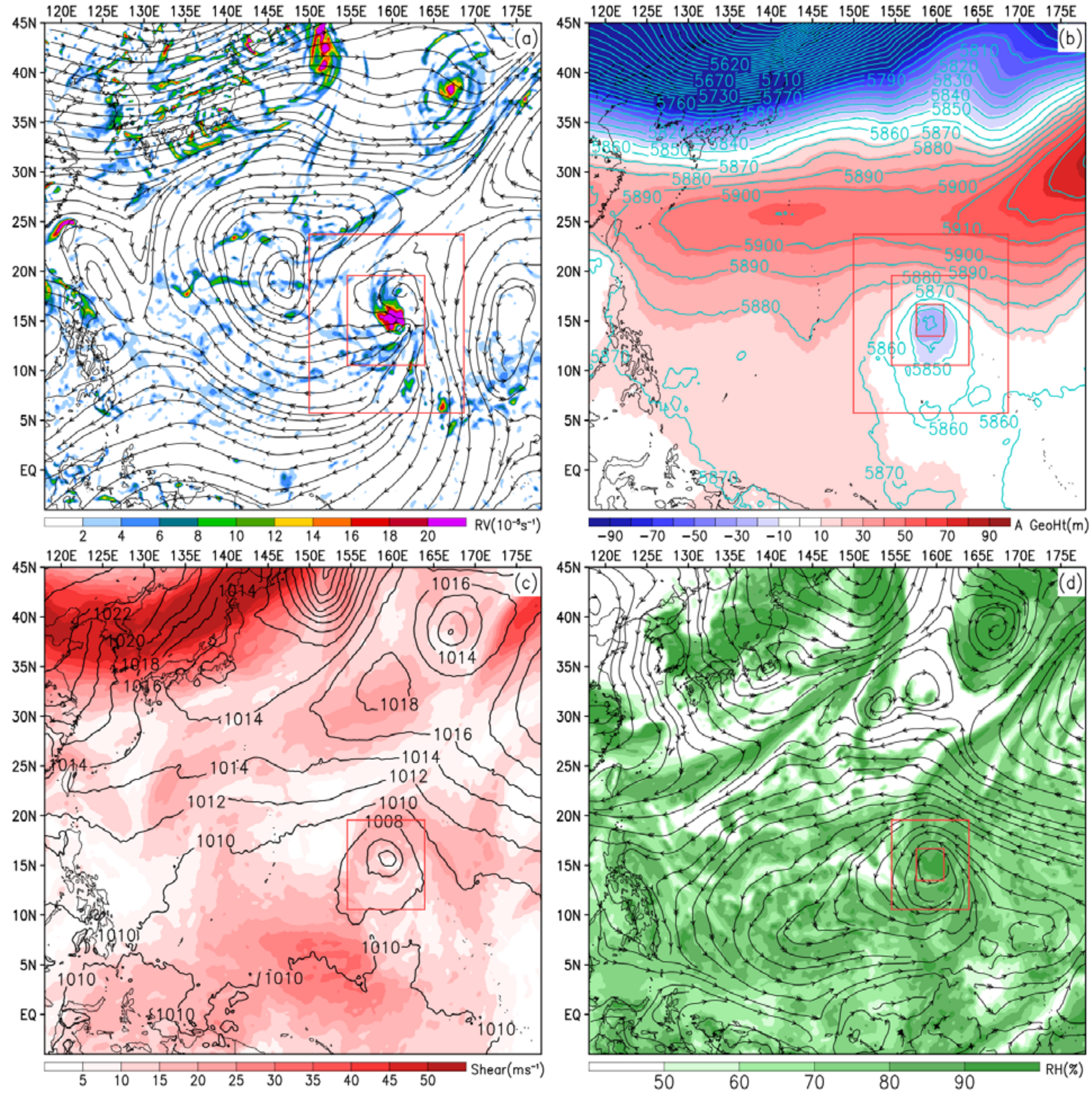

Fig. 2. (a) 850-hPa relative vorticity (10^{-5} s^{-1}, shaded,), and 200-hPa winds (stream), (b) 500-hPa geopotential height (contours, m) and its anomaly (m, shaded), (c) 200–850 hPa vertical wind shear (m s^{-1}, shaded) and sea level pressure (hPa, contours) and (d) 850-hPa relative humidity (%) and winds (stream), for the environment of Typhoon Hagibis at the model initial time of 1200 UTC 5 Oct. 2019. The moving nests from four experiments are shown in (a) Q36km3, (b) Q36km4, (c) Q12km2 and (d) Q12km3, respectively.

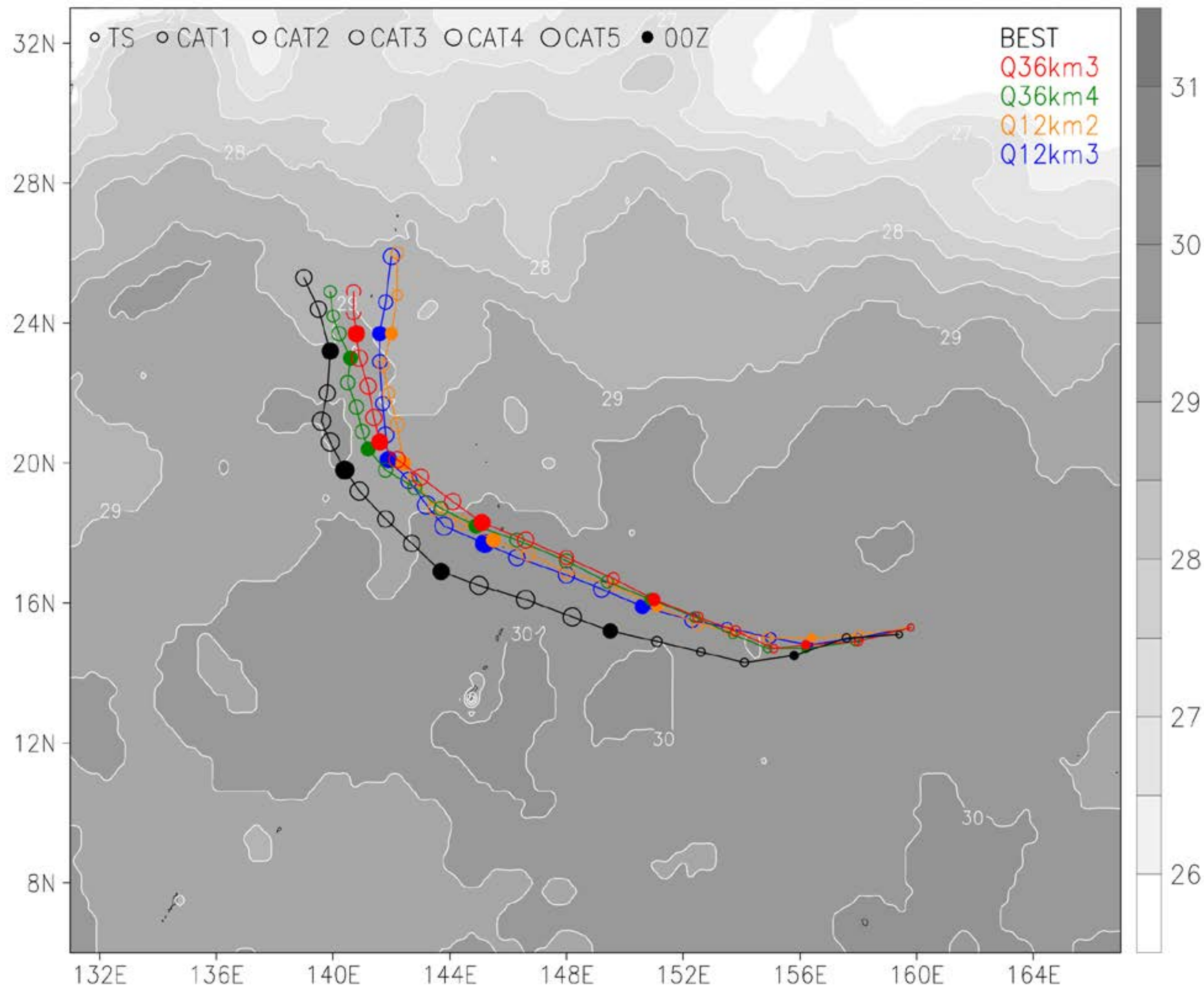

Fig. 3. Comparison of track forecasts with the best-track (black) for Typhoon Hagibis, from the sensitivity experiments initialized at 1200 UTC 5 Oct. 2019, overlaid with the sea surface temperature (^{0}C, gray shaded and contours) at the model initial time. The dots are for the storm locations every 6-h.

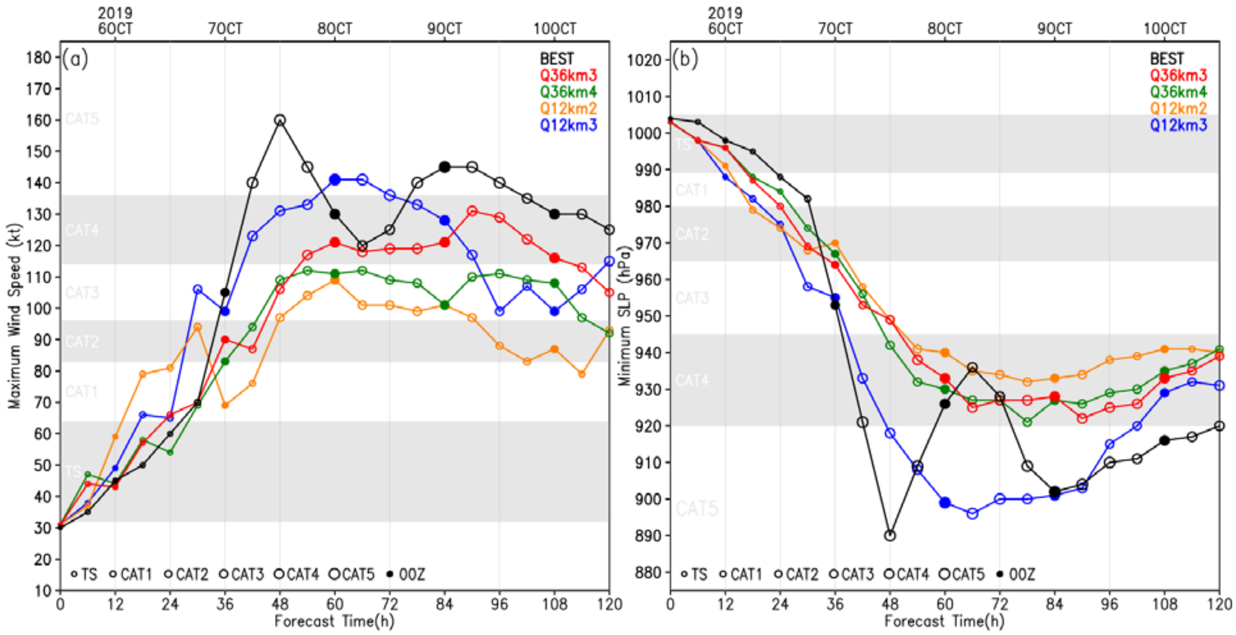

Fig. 4. Comparison of multi-model real-time intensity forecasts starting at 1200 UTC 5 Oct. 2019 with the revised best-track (black) for Typhoon Hagibis: (a) MWS (kt, 1 kt = 0.51444 m s^{-1}) and (b) MSLP (hPa).

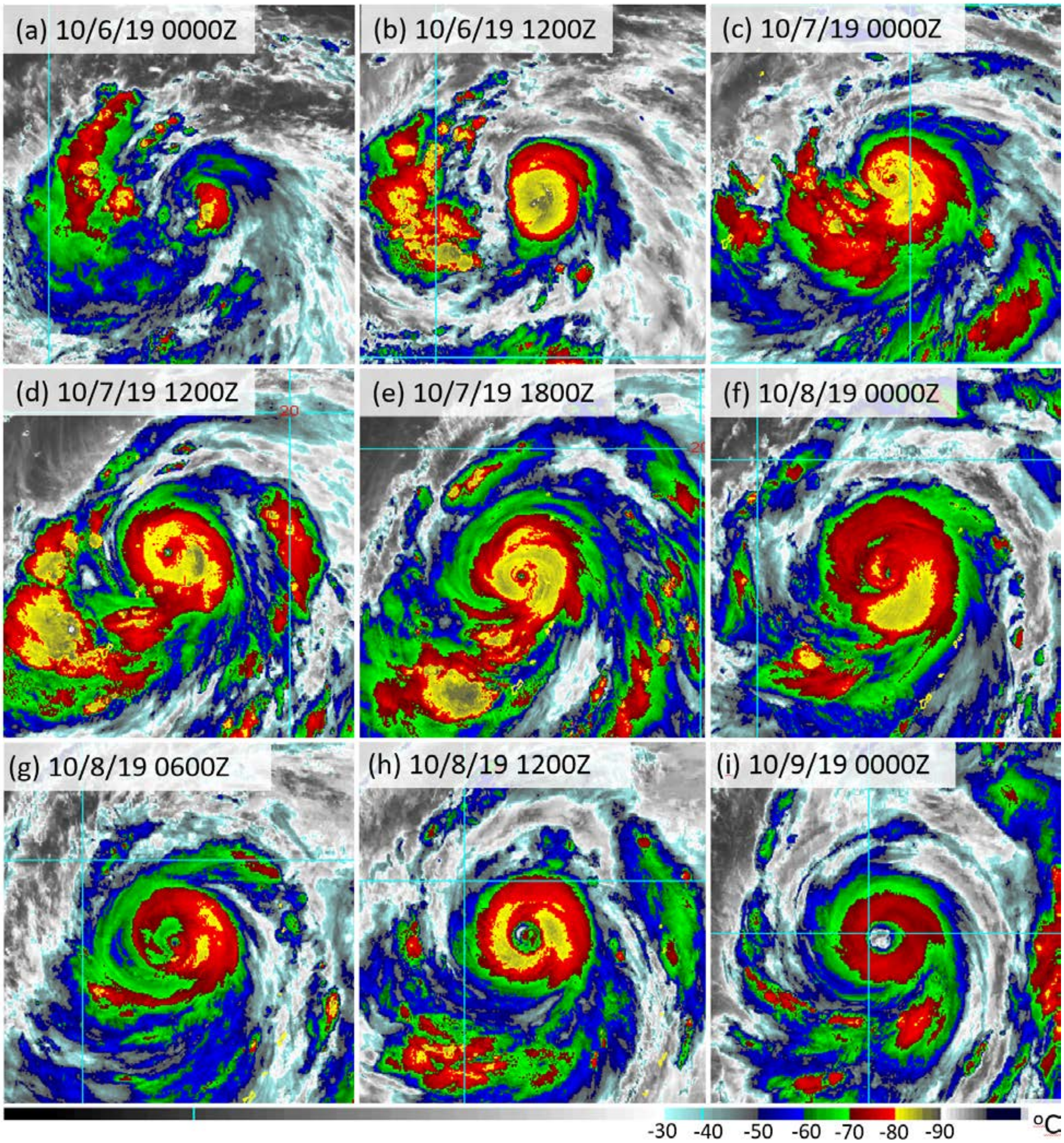

Fig. 5. Himawari-8 enhanced infrared (IR) temperatures (°C)of Typhoon Hagibis (20W 2019) at (a) 0000 UTC 6 Oct., (b) 1200 UTC 6 Oct., (c) 0000 UTC 7 Oct., (d) 1200 UTC 7 Oct., (e) 1800 UTC 7 Oct., (f) 0000 UTC 8 Oct., (g) 0600 UTC 8 Oct., (h) 1200 UTC 8 Oct., and (i) 0000 UTC 9 Oct. 2019. Each panel has a size of 10x10 degrees in latitude and longitude.

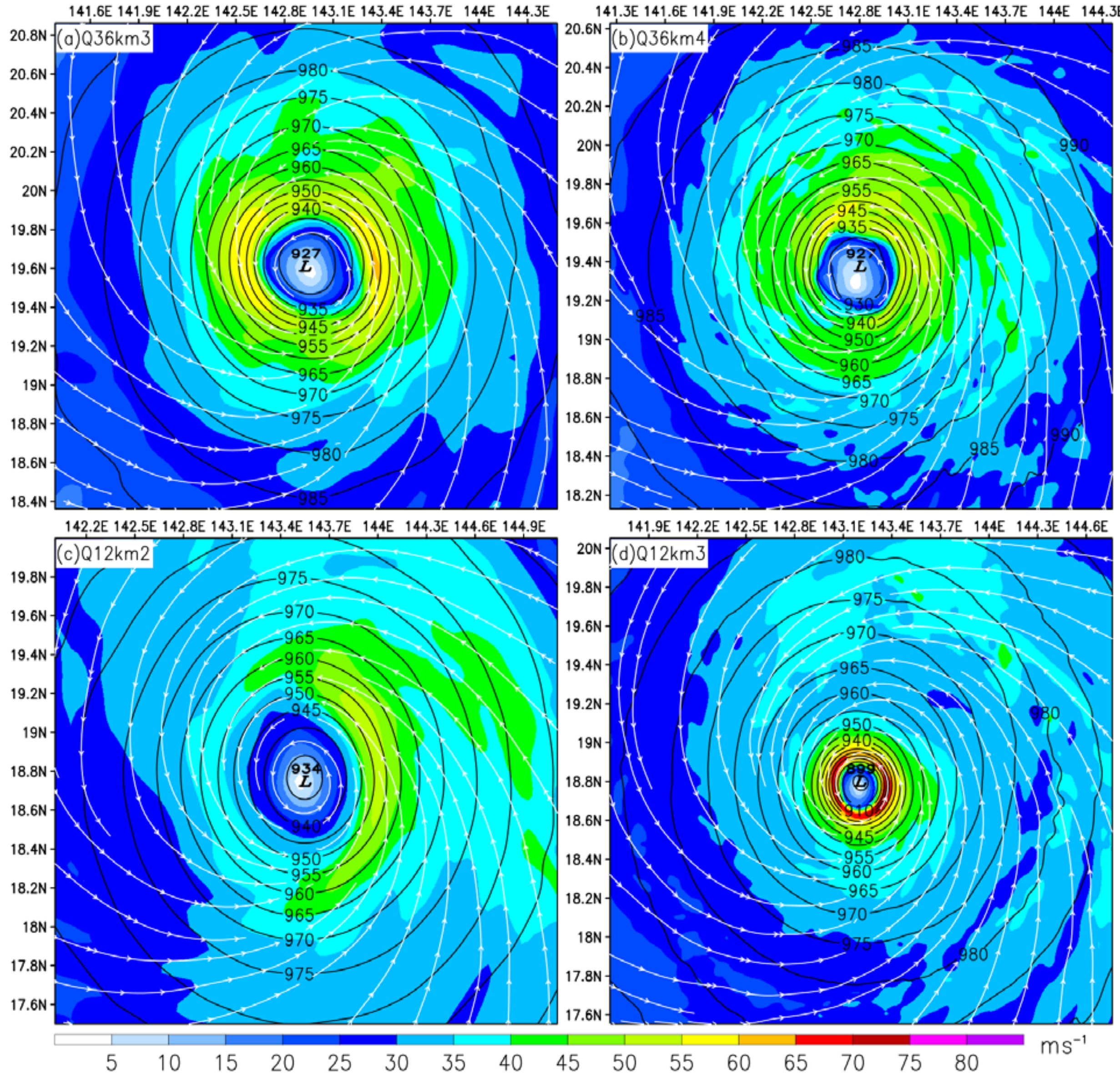

Fig. 6. The 10-m winds (m s^{-1}, shaded and streamlines), and sea-level pressure (hPa, black contours) at 72-h for four experiments (a) Q36km3, (b) Q36km4, (c) Q12km2, (d) Q12km3, from the forecasts starting at 1200 UTC 5 Oct. 2019.

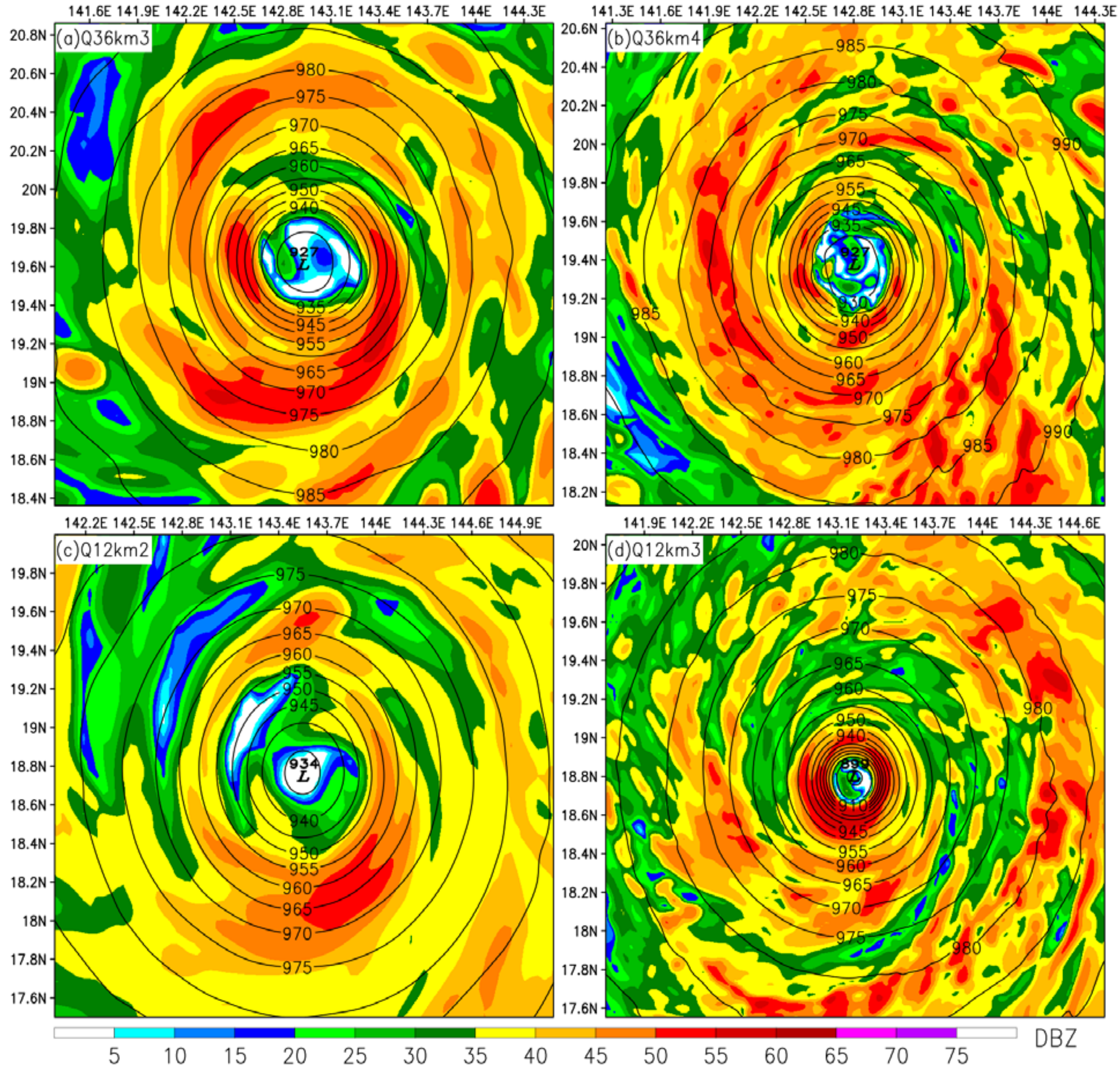

Fig. 7. The simulated composite radar reflectivity (DBZ, shaded), and sea-level pressure (hPa, contours) at 72-h for four experiments (a) Q36km3, (b) Q36km4, (c) Q12km2, (d) Q12km3, from the forecasts starting at 1200 UTC 5 Oct. 2019.

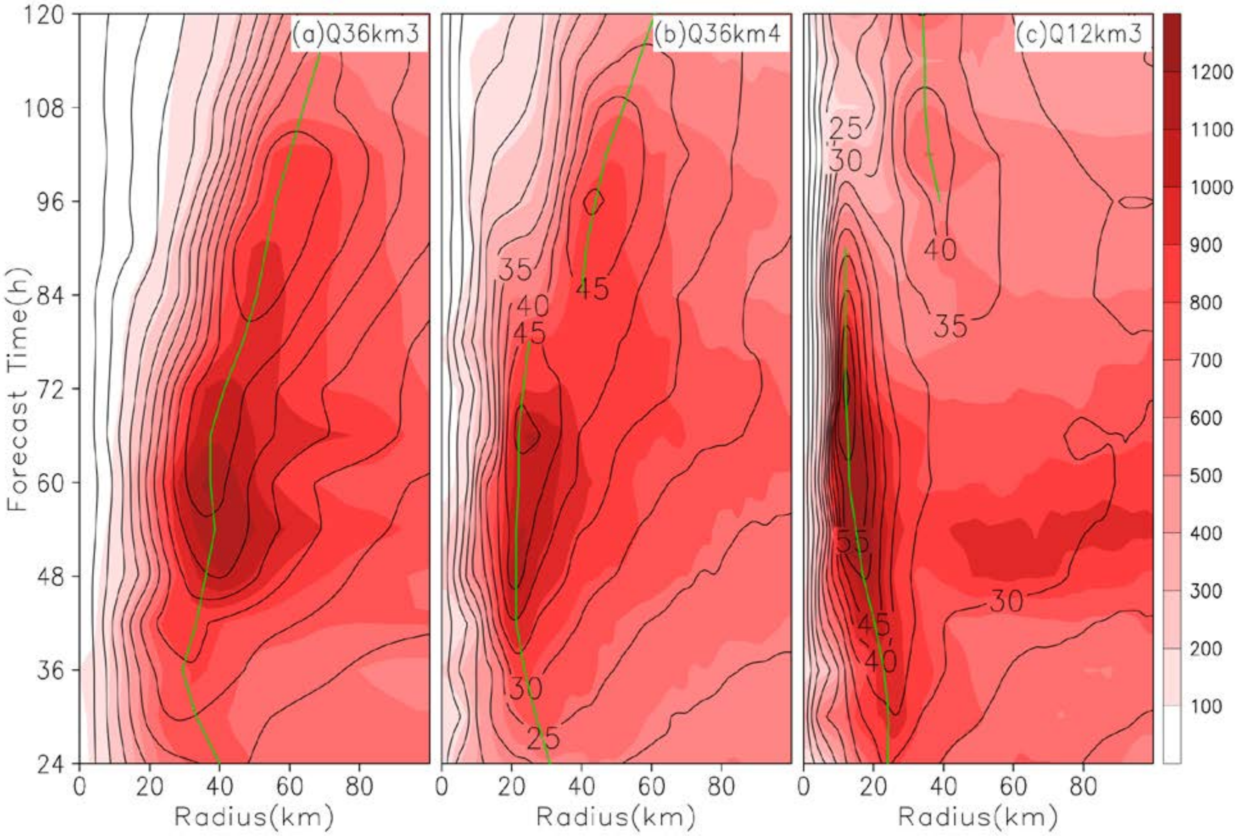

Fig. 8. Radius-time plots of the azimuthally averaged surface latent heat flux (W m^{-2}, shaded), 10-m wind speed (m s^{-1}, black contours at 5 interval) and the radius of maximum wind speed (km, green line) for experiments (a) Q36km3, (b) Q36km4, (c) Q12km3.

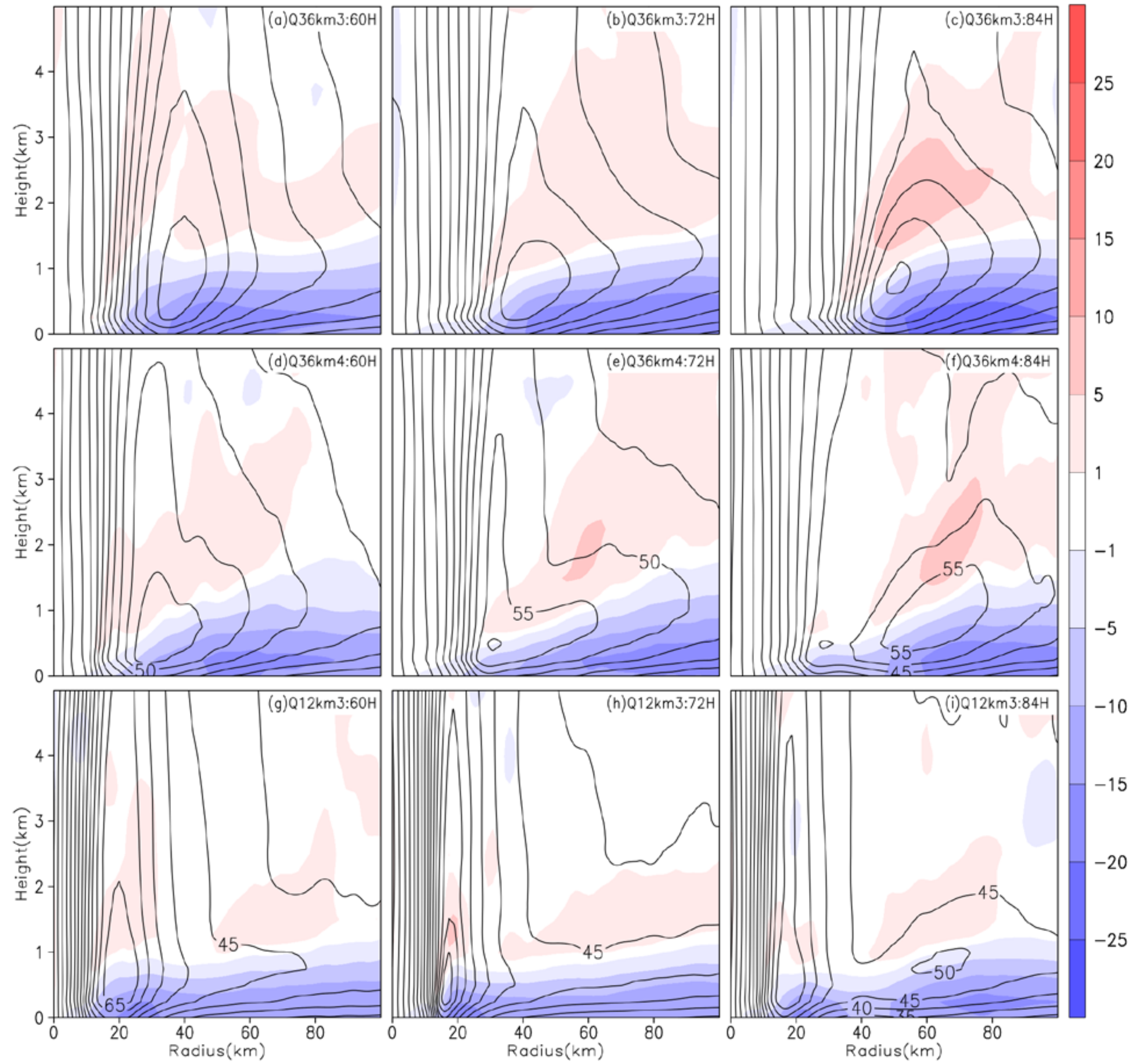

Fig. 9. Radius-height plots of the azimuthally averaged radial winds (m s^{-1}, shaded), tangential winds (m s^{-1}, black contours at 5 interval) for experiments (a-c) Q36km3, (d-f) Q36km4, (g-i) Q12km3, at 60 h, 72 h, and 84 h respectively.

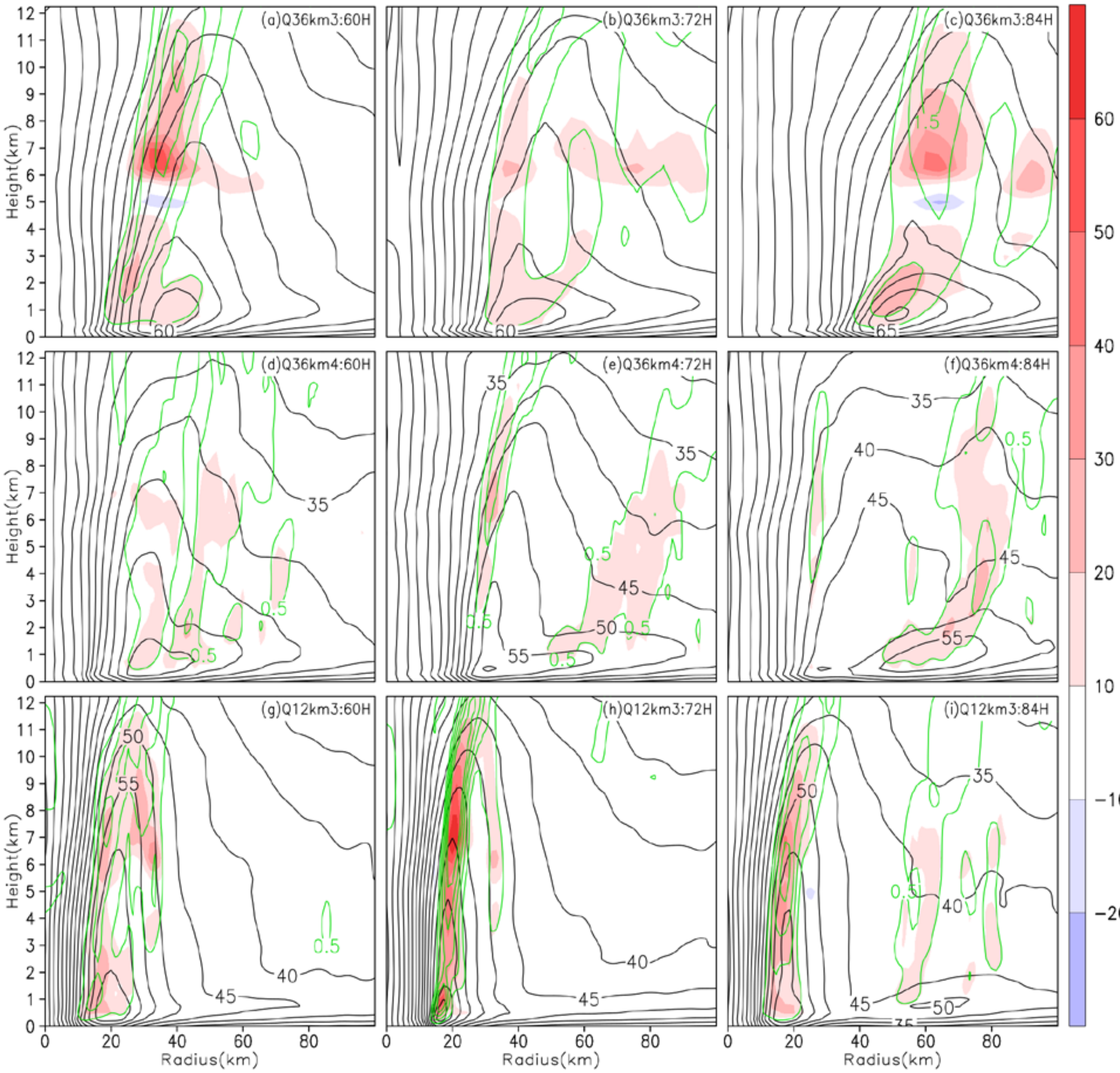

Fig. 10. Radius-height plots of the azimuthally averaged diabatic heating rate (K h^{-1}, shaded), tangential winds (m s^{-1}, black contours at 5 interval) and vertical velocity (m s^{-1}, green contours at 0.5 interval) for experiments (a-c) Q36km3, (d-f) Q36km4, (g-i) Q12km3, at 60 h, 72 h, and 84 h respectively.

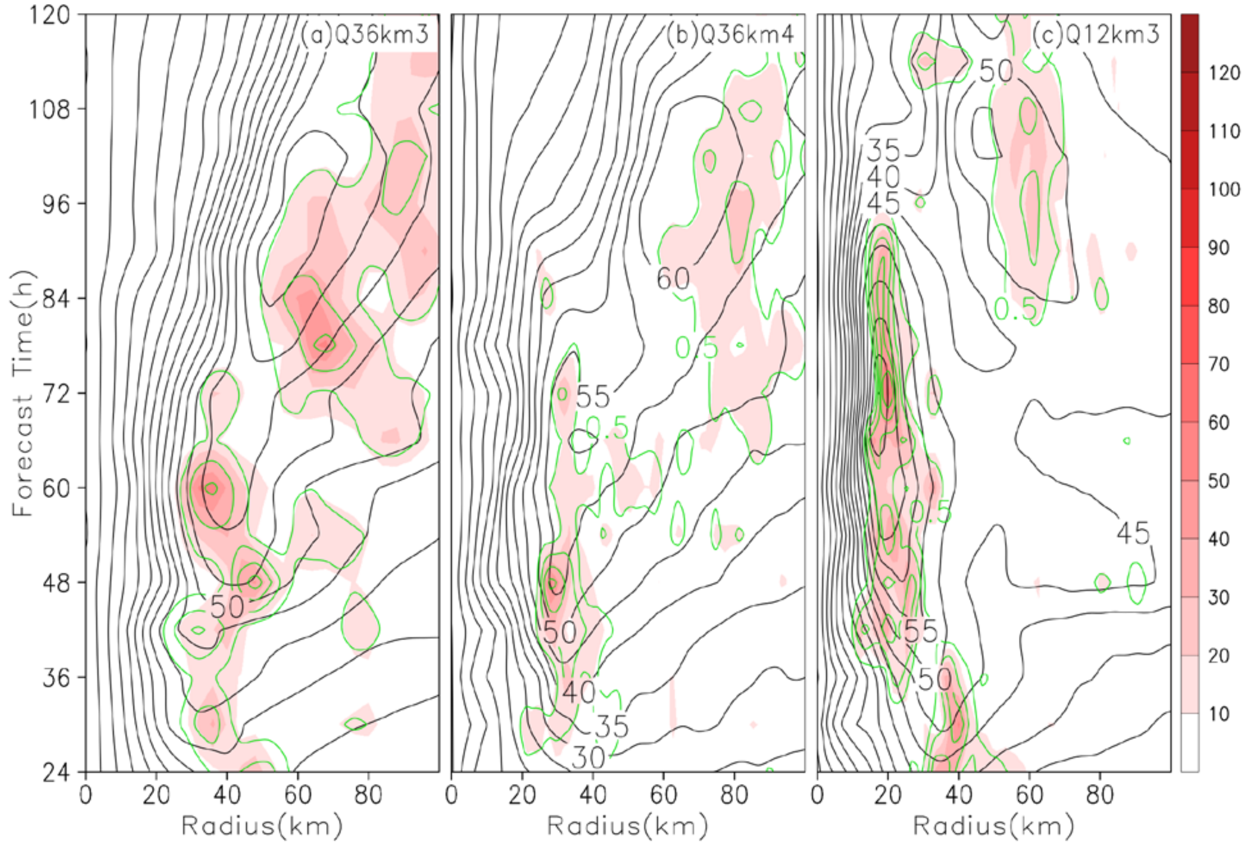

Fig. 11. Radius-time plots of the azimuthally averaged diabatic heating rate (K h^{-1}, shaded) and vertical velocity (m s^{-1}, green contours at 0.5 interval) at 6.5 km height, and tangential winds (m s^{-1}, black contours at 5 interval) at 1-km, from experiments (a) Q36km3, (b) Q36km4, (c) Q12km3.

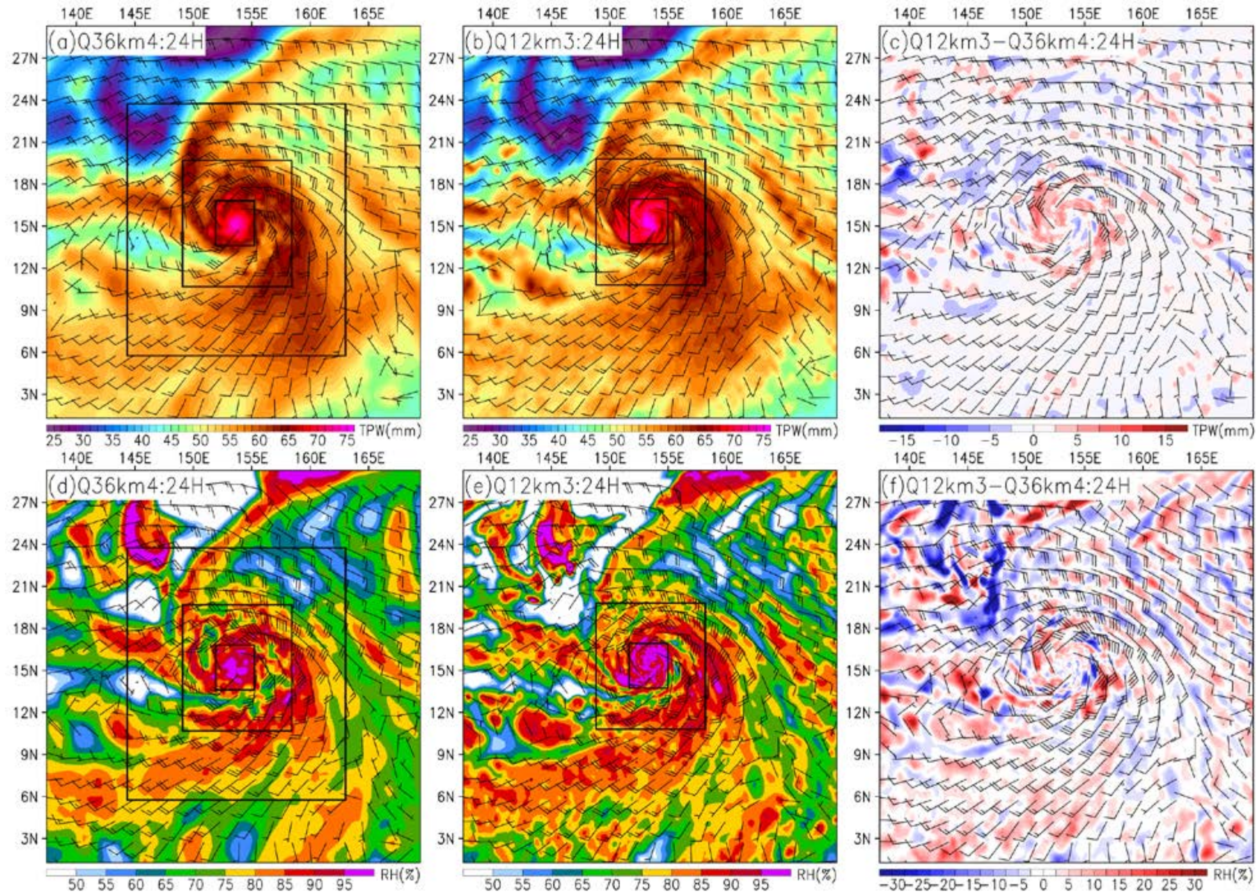

Fig. 12. Comparison of the environmental fields from the experiments Q36km4 (a,d), Q12km3 (b,e) and their differences (c,f) for Typhoon Hagibis at 24-h from the fixed outer grid: (a-b) total precipitable water (TPW, mm, shaded) and the averaged winds (kt, barb, 1 kt = 0.51444 m s^{-1}) from surface to 850-hPa; (c) the TPW difference (mm, shaded) and the averaged winds (kt, barb) of surface to 850 hPa from two experiments; (d-e) relative humidity (%, shaded) and 850-hPa winds (kt, barb); and (f) the relative humidity difference (%, shaded) and the averaged 850-hPa winds (kt, barb) from two experiments. The moving nests in the experiments are shown as the black frames.

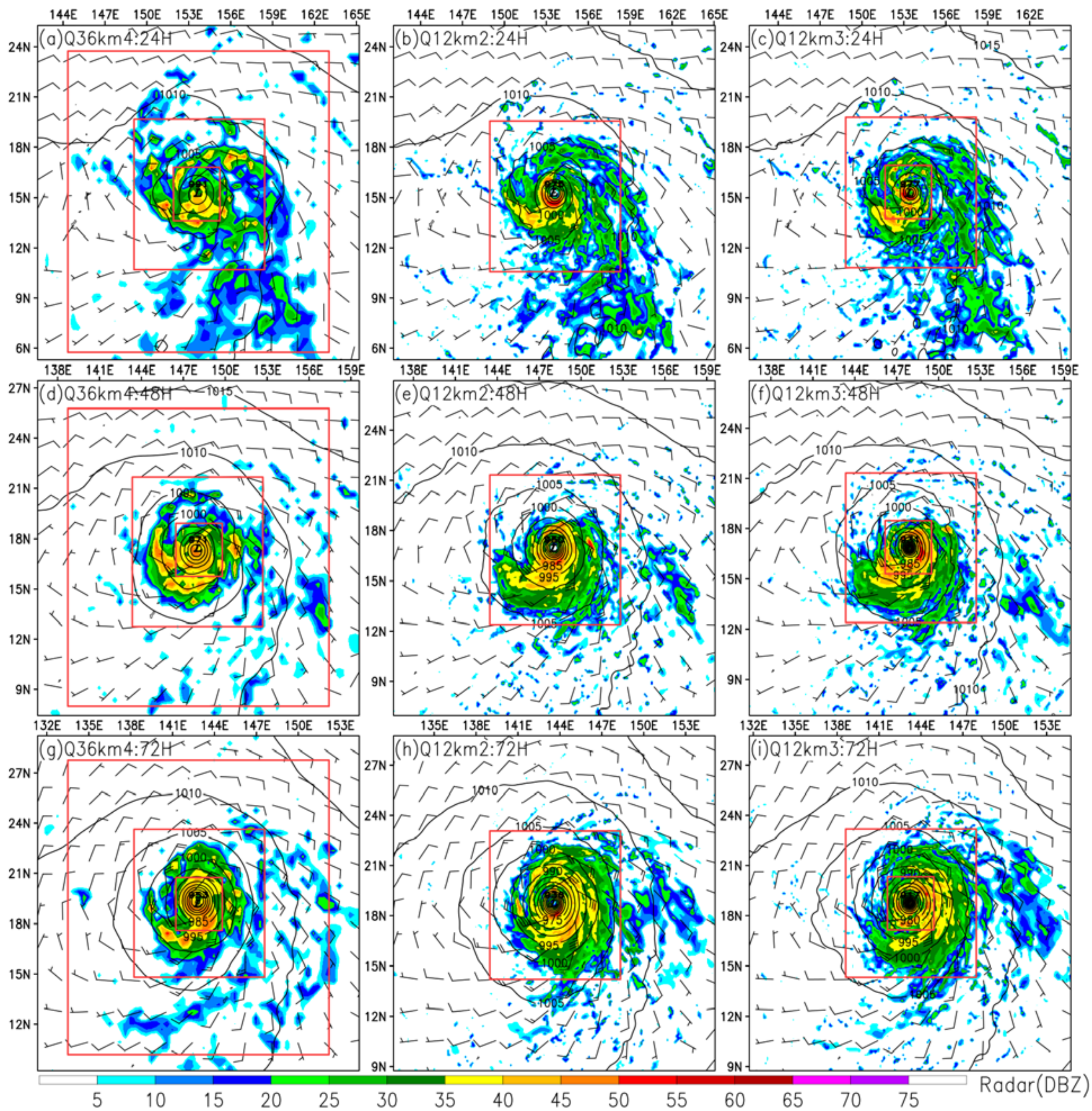

Fig. 13. Comparison of simulated composite radar reflectivity (DBZ, shaded), sea-level pressure (hPa, contours) and 10-m winds (m s^{-1}, barb) for Typhoon Hagibis at 24-h, 48-h and 72-h from the fixed outer grid of experiments (a,d,g) Q36km4 at 36-km, (b,e,h) Q12km2 and (c,f,i) Q12km3 at 12-km.. The moving nests in the experiments are shown as the red frames.

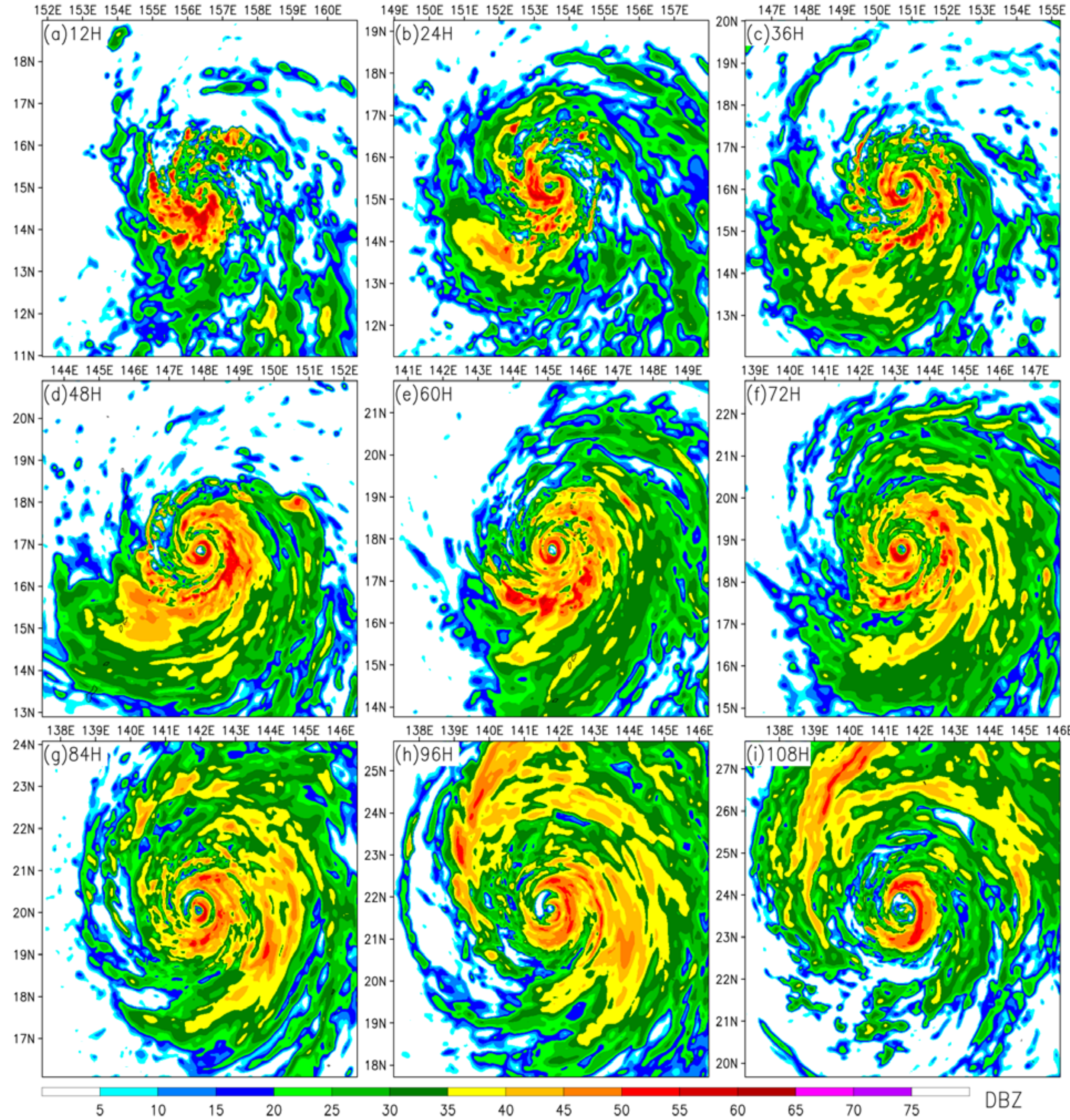

Fig. 14. The simulated composite radar reflectivity (DBZ, shaded) of Typhoon Hagibis at (a) 12-h, (b) 24-h, (c) 36-h, (d) 48-h, (e) 60-h, (f) 72-h, (g) 84-h, (h) 96-h and (i) 108-h from the experiment Q12km3, starting at 1200 UTC 5 Oct. 2019.